Universität Zürich^{UZH}

ETH
Eidgenössische Technische Hochschule Zürich
Swiss Federal Institute of Technology Zurich

Optimization of a Deuterium Negative Ion Source for Ion Trapping

Master's Thesis

Reza Mosala Nejad

December 9, 2021

Advisors: Prof. Titus Neupert, Dr. Daniel Kienzler

Department of Physics, UZH, ETH Zürich

Acknowledgements

First of all, I would like to thank my dear family for their tremendous support during my master's study in physics. Mom, dad, and my dear sister, this would not have been possible without you.

I would also like to thank my advisor Daniel Kienzler whose expertise was invaluable in the progression of this project. I would also like to acknowledge my co-advisor Nick Schwegler, and my master's thesis partner Matteo Simoni. Our conversations massively helped me in making the right decisions in relation to the the experiments I did, and also the interpretation of the results.

I would like to thank Prof. Titus Neupert for taking the responsibility of being my advisor from UZH's side, and offering us his precious time to become engaged in this project.

Finally, I would like to express my gratitude towards Prof. Jonathan Home for giving me the opportunity to do my master's thesis at his prestigious group TIQI, ETHZ.

Abstract

A deuterium negative ion source for ion trapping was studied and upgraded. Deuterium negative ions are created through a surface process by shooting electrons at a tungsten grid in a vacuum chamber filled with deuterium gas. The amount of the extracted D^- ions increased linearly with the grid negative voltage up to 1 kV. The optimum electron energy was found to be around 200 eV. The impact of Cs deposition on the grid in relation to the D^- ion production was also studied. In this study, developments were made to the electronics and the control system of the existing setup. The setup was also upgraded with the addition of two newly designed e-guns and a Cs dispenser.

Contents

Chapter 1

Introduction

The aim of this project from producing D^- ions is for them to be used in trapped ion experiments. There are two motivations for using D^- ions in such experiments: quantum information processing, and quantum metrology.

1.1   Quantum Information Processing

Using trapped ions is perceived to be a possible way of building quantum information processors. One of the proposed architectures to implement trapped ion quantum computing is QCCD[1] architecture. In this architecture different qubit ions are placed in different traps with another ion responsible for cooling and state readout. To operate quantum gates among these separate qubit ions, they need to be brought together in a single trap so that they form an entangled state. However, for this operation to happen, the trap potential needs to be changed into an x^4 shape (Fig. 1.1a). To create such a potential, voltages of the order of 10^2 V need to be applied to the trap electrodes. This causes technical difficulties for the trap electrodes insulation. Moreover, as the qubit ions move into a single trap, the trap frequency temporarily decreases (Fig. 1.1a). This drop in the trap frequency results in more heating rate on the qubit ions. Consequently, the coherence time in the entangled-ions system drops as well.

A possible solution to the low trap frequency problem is to put the ions always in separate traps while keeping them coupled (Fig. 1.1b). However, to couple the ions strongly they need to be close to each other. On the other hand, the inter-ionic distance is dependent on their distance from the trap electrodes; the smaller the inter-ionic distance, the smaller the ions distance

---

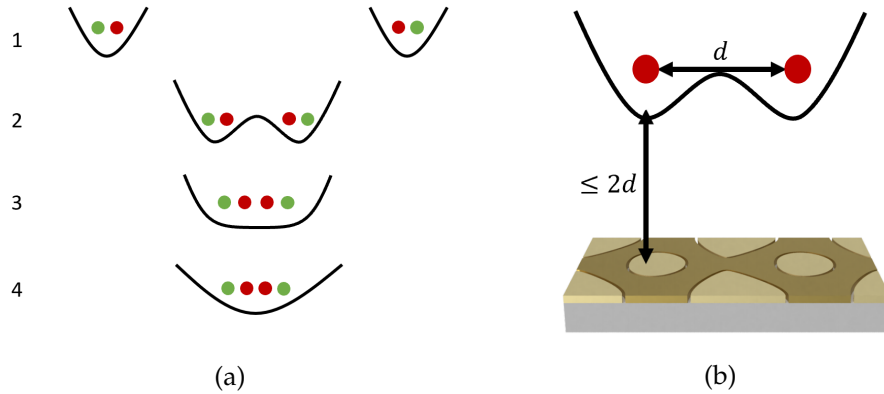[1]QCCD stands for quantum charged coupled device.

Figure 1.1: **(a)** Transfer of ions in a QCCD architecture. Each trap in the QCCD architecture holds two ions: one as the qubit, and the other as the ancillary ion for cooling and readout. Stages 1 to 4 show how two traps merge into a single trap. Stage 3 illustrates when the trap frequency drops. **(b)** Illustration of the fact that the inter-ionic distance and the trap-to-ion distance are related together.

to the trap electrodes is. However, smaller trap-to-ion distance results in higher heating rate of the ions, and consequently lower coherence time.

One possible solution to this problem, is that negative and positive ions be used together, so that the negative ions store the qubits and the positive ions be used for cooling, state readout, and as a mediator for the coupling of the negative ions (Fig. 1.2a, 1.2b). This way, negative ions never come into direct coupling, so there will be no need for an x^4 potential. Instead, the potential would have an x^3 shape. To make such a trap potential, lower voltages (~ 10 V) need to be applied to the trap electrodes, and there will be no drop in the trap frequency either as the ions are always in separate potential wells.

Even though negative ions can possibly solve the excessive heating rate and high voltage issues, there are massive challenges in the use of negative ions. The main issue is that atomic negative ions are very unstable, and easily lose their extra electron under laser radiation. Molecular negative ions are also an option to think of; however, they possess a great number of degrees of freedom which make their cooling and trapping quite challenging.

1.2 Quantum Metrology

Trapped ions can be used for quantum logic spectroscopy (QLS) as well [2]. In QLS two ion species are co-trapped. One ion is called the spectroscopy ion which is the ion that its transitions are measured. The other ion, called the logic ion, is an ion with suitable transitions for efficient laser cooling,
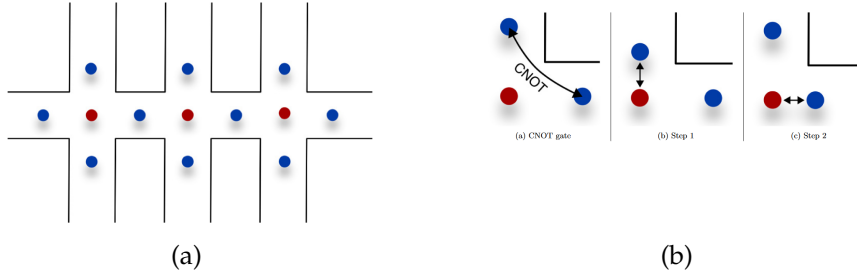
Figure 1.2: **(a)** Schematic illustration of the proposed QCCD architecture with negative qubit (blue) and positive ancillary ions (red). The picture is taken from [1]. **(b)** Schematic illustration of performing a CNOT quantum operations on two negative ions through a positive ion. The picture is taken from [1].

internal state preparation, and detection like Be^+ [2]. The complete control over the logic ion can be used to measure the chosen transition in the spectroscopy ion with great precision. The procedure is as follows. First, the two ions are prepared in the motional ground state with Doppler and sideband cooling. Then, with a coherent pulse of laser tuned close to the spectroscopy ion transition, it is put into a superposition state (Eq. 1.1). Then, with a π red sideband (π-RSB) pulse to the spectroscopy ion, this superposition is encoded into the motional state of the ions (Eq. 1.2). Then, with a π-RSB pulse on the logic ion, this motional superposition state is encoded to the logic ion internal electronic states (Eq. 1.3). Then, with state-dependent fluorescence the population of the logic ion electronic state is measured. This procedure is repeated many times to collect statistics, and Rabi spectroscopy can be done to find the spectroscopy ion transition frequency. Fig. 1.3b shows the Rabi spectroscopy for a transition in $^{27}Al^+$ ion co-trapped with Be^+ ion.

$$\Psi_0 \rightarrow \Psi_1 = (\alpha \left|\downarrow\right\rangle_S + \beta \left|\uparrow\right\rangle_S) \left|\downarrow\right\rangle_L \left|0\right\rangle_m = (\alpha \left|\downarrow\right\rangle_S \left|0\right\rangle_m + \beta \left|\uparrow\right\rangle_S \left|0\right\rangle_m) \left|\downarrow\right\rangle_L \quad (1.1)$$

$$\Psi_1 \rightarrow \Psi_2 = (\alpha \left|\downarrow\right\rangle_S \left|0\right\rangle_m + \beta \left|\downarrow\right\rangle_S \left|1\right\rangle_m) \left|\downarrow\right\rangle_L = \left|\downarrow\right\rangle_S \left|\downarrow\right\rangle_L (\alpha \left|0\right\rangle_m + \beta \left|1\right\rangle_m)$$
$$(1.2)$$

$$\Psi_2 \rightarrow \Psi_{final} = \left|\downarrow\right\rangle_S (\alpha \left|\downarrow\right\rangle_L + \beta \left|\uparrow\right\rangle_L) \left|0\right\rangle_m \quad (1.3)$$

QLS provides great accuracy in measuring the atomic transitions. Since the transitions are dependent on the fundamental physical constants like the
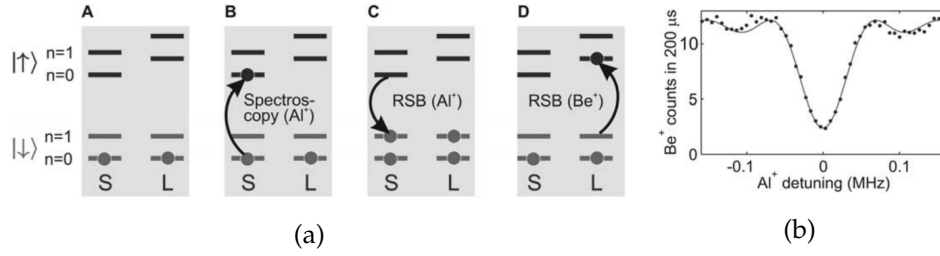
3

(a)   (b)

Figure 1.3: **(a)** Spectroscopy and transfer scheme for spectroscopy (S) and logic (L) ions sharing a common normal mode of motion, the transfer mode, with excitation n. (Only the ground and first excited states of the transfer mode are shown.) (A) Initialization to the ground internal and transfer-mode states. (B) Interrogation of the spectroscopy transition. (C) Coherent transfer of the internal superposition state of the spectroscopy ion into a motional superposition state by use of an RSB π pulse on the spectroscopy ion. (D) Coherent transfer of the motional superposition state into an internal superposition state of the logic ion by use of an RSB π pulse on the logic ion. The picture is taken from [2]. **(b)** Rabi spectroscopy of the $\left|{}^1S_0, F = 5/2, m_F = 5/2\right\rangle \rightarrow \left|{}^3P_1, F' = 7/2, m'_F = 7/2\right\rangle$ transition in ${}^{27}Al^+$, showing a frequency scan across the resonance. The data (black circles) are fit by the theoretically expected probability $P_{\downarrow,S}$ of finding ${}^{27}Al^+$ in the ground state after applying the probe pulse. The picture is taken from [2].

electron mass, QLS provides a way to do quantum metrology[2]. One of the applications of QLS in the context of quantum metrology is testing theories like CPT theorem. Charge, parity, and time reversal symmetry is a fundamental symmetry of physical laws under the simultaneous transformations of charge conjugation, parity transformation, and time reversal. However, there are theories that predict CPT violation. There has been increasingly preciser tests on the magnetic moments of proton and anti-proton trapped in a penning trap [3, 4]. To increase the accuracy of comparison between electron (proton) and positron (anti-proton) properties, there has been the suggestion of doing QLS on H_2^+ and its antimatter ($\overline{H_2^-}$) [5]. To do QLS on H_2^+ and $\overline{H_2^-}$ each one needs to be co-trapped with a well-known ion like Be^+ or Ca^+. At TIQI there is an ongoing project to co-trap H_2^+ and Be^+ ions called the "Molecules" project. The co-trapping of $\overline{H_2^-}$ is, of course, more ambitious and challenging. In this project, the "Negative Ions" project, the purpose is to co-trap Be^+ with D^- which is the closest ion in mass to $\overline{H_2^-}$, and consequently needs a trap with identical characteristics (Fig. 1.4). To

---

[2]Metrology is the science of measurement of fundamental physical constants. Quantum metrology is a branch of metrology where the techniques in quantum science, e. g., trapped ions are used for measurement.
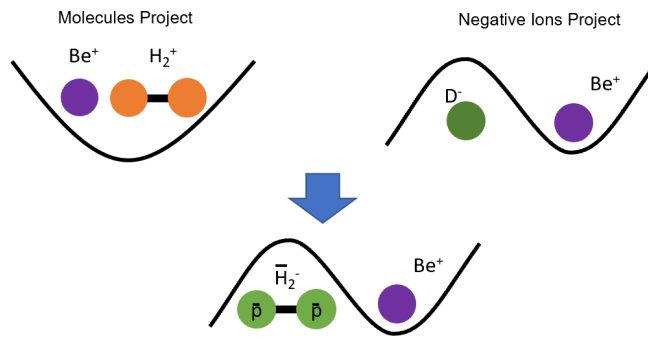
Figure 1.4: Position of the negative ions, and the molecules projects in relation to the QLS of H_2^+ and $\overline{H}_2^-$.

sum up, this project is the first step towards the realization of the QLS of H_2^+ and $\overline{H}_2^-$. With co-trapping a negative and positive ion, this project is also the first step towards a positive - negative ion QCCD architecture.

5

Chapter 2

Review of D^- Ion sources

The more D^- ions are produced, the more chance there is to trap them. This was the motivation to try all possible ways through which the D^- ion production rate is enhance. To do so, it is necessary to know the key factors and the processes that lead to D^- ion production. Because of similar electronic configuration of deuterium and hydrogen, these processes are similar for both H^- and D^- ion formation. Hence, on a qualitative level, all the information on the H^- ion formation can also be used for D^- [6]. On a quantitative level, H^- ion formation is proved to be more efficient no matter what the process is [6]. In the following these processes are briefly discussed.

For a D^- ion to be formed, the deuterium atom needs to gain an extra electron. Based on how this electron attachment takes place, D^- ion sources are divided into two types: volume sources, and surface sources [6].

2.1 Volume Sources

In general, inelastic scattering of deuterium atoms (D), molecules (D_2), or positive ions (D^+, D_2^+, D_3^+) with other particles can result in the formation of D^- through transfer of electrons. The other scattering particles in this scattering process can be anything, ranging from electrons to deuterium or other species of atoms molecules or ions. Here are some examples of the volume processes for D^- formation.
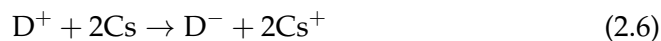
$$e + D \rightarrow D^- + h\nu \tag{2.1}$$

$$e + D_2 \rightarrow D^- + D \tag{2.2}$$

$$e + D_2 \rightarrow e + D^- + D^+ \tag{2.3}$$

$$e + D_2^+ \rightarrow D^- + D^+ \tag{2.4}$$

$$D_2^+ + D_2 \rightarrow D^- + D + 2D^+ \tag{2.5}$$

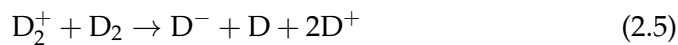$$D^+ + 2Cs \rightarrow D^- + 2Cs^+ \tag{2.6}$$

Figure 2.1: Schematic illustration of a double charge exchange source. The picture is taken from [6].

2.1.1 Double Charge Exchange Sources

The key for these inelastic scatterings to result in D^- ion formation is that the electron affinity (EA) of deuterium be higher than the electron affinity of the other scattering particles. For example, D^- ion can not be expected to be formed from the interaction between deuterium ($EA_D = 0.7546$ eV) and oxygen ($EA_O = 1.4611$ eV), but D^- ion can be easily formed from the interaction of D^+ ion ($EA_D = 0.7546$ eV) and caesium atom ($EA_{Cs} = 0.4716$ eV) as represented in Eq. 2.6. Cs atom has the tendency to lose its valance electron to reach the octet configuration while the D^+ ion can attract two electrons: one electron to reach the atomic ground state and release the 15.47 eV ionization energy, and an extra electron to reach the D^- state and release the 0.7546 eV affinity energy. Using alkali metals vapor to create D^- ions has been implemented before [7]. The working principle is depicted in Fig. 2.1. A beam of D^+ ions (~ 1 kV), which can easily be created through electric discharge, is passed through the alkali metal vapor ($\sim 10^{-3}$ mbar) where the inelastic scattering and two-electron charge transfer takes place. Hence this type of D^- ion source is called double charge exchange source. The kinetic energy of the incoming beam of D^+ ions is necessary to provide the activation energy for the electron transfer from the Cs atoms to D^+ ions. Very high currents (of the order of amperes) of D^- ions have been reported using this technique [6].

2.1.2 Volume Plasma Sources

Eq. 2.2 describes dissociative electron attachment (DEA) which has been extensively explored during the past several decades. In Fig. 2.2a the cross-section of DEA for hydrogen (red) and deuterium (black) are presented. Three resonances can be observed in the DEA cross-section: one resonance around 4 eV, another within 7 eV to 13 eV, and another one around 14 eV. This cross-section can be massively enhanced through the vibrational excitation of the deuterium molecules. Fig. 2.2b shows how the cross-section of the 4 eV DEA resonance enhances with the vibrational excitation of the

molecules. The 14 eV resonance, however, increases at most by a factor of 20 with the vibrational excitation[1] [8]. Hence vibrational excitation of D_2 molecules is a key factor to enhance the probability of DEA. Fig. 2.3a illustrates that electrons of energies above 20 eV can efficiently vibrationally excite H_2 molecules.

There is also another process which leads to vibrational excitation of D_2 molecules. It is referred to as dissociative adsorption and recombination. In this process D_2 molecules adsorb on the surface, and as they adsorb they dissociate into deuterium atoms. These deuterium atoms can associate again, and form a vibrationally excited molecule as they desorb from the surface. This process happens on the chamber walls; however, this mechanism only boosts the D^- production roughly by a factor of 2 [9].

Therefore, to efficiently use the DEA, electrons of > 20 eV and < 5 eV are needed for D_2 vibrational excitation, and ignition of the 4 eV DEA resonance respectively. This can be achieved by creating a plasma through hot filament discharge as depicted in Fig. 2.4a. It is enough to keep the filaments at about 50 V voltage difference, then the primary electrons can vibrationally excite, ionize, and cause polar dissociation (Eq. 2.3) of the deuterium molecules (Fig. 2.3b). As a result, the primary electrons lose their energy and thermalize at some temperature of the order of $k_B T \sim 1$ eV which is the right temperature to maximally use the 4 eV vibrationally enhanced DEA resonance [10]. As this plasma is the necessary element in the source operation, these sources are called volume plasma sources. These sources like the double charge exchange sources also produce high currents of D^- ions (Fig. 2.4b).

There are some key factors for this type of D^- source to work.

- To create D^- ions it is necessary to form the plasma. **Plasma provides a large interaction environment** among electrons of different energies, and deuterium molecules and ions, and keep them in interaction via Coulomb force.

- The presence of a confining magnetic field at the plasma is also crucial. Otherwise, ions and electrons keep escaping from the plasma and weaken the interaction. Moreover, low energy electrons and positive ions could also diffuse to the extraction area (Fig. 2.4a), and mix up with the negative ion beam.

- Even though these sources work in low pressure plasma, i. e., $\sim 10^{-3}$ mbar, high-vacuum pressure, i. e., $< 10^{-5}$ mbar would inevitably result in much less interaction, hence lower D^- production rate.

- As a rule of thumb, higher discharge currents produce higher D^- currents until it saturates (Fig. 2.4b).

---

[1]The 7-13 eV resonance dependence on vibrational excitation has not been studied.
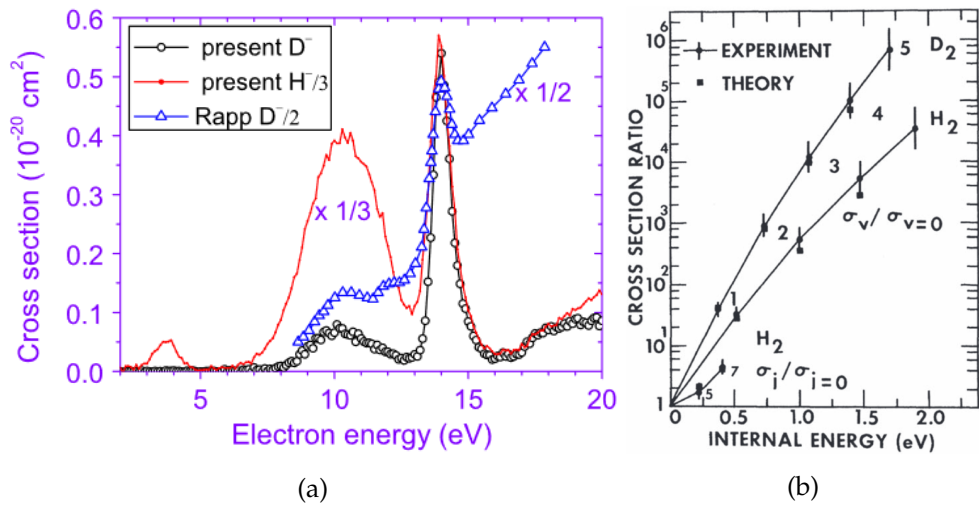
(a)   (b)

Figure 2.2: **(a)** DEA cross-section versus the electrons energy. The red curve represents the DEA cross-section for H^- formation, the black for D^-, and the blue represents some older measurement for D^-. The picture is taken from [11]. **(b)** Internal state dependence of DEA cross-sections in H_2 and D_2 via the 4 eV resonance. The ground state cross-sections (at 300 K) are 1.6×10^{-21} cm^2 for H_2 and 8×10^{-24} cm^2 for D_2. Note that the cross-section enhancement by vibrational excitation (index v) is much larger than that by rotational excitation (index i) at the same internal energy. The picture is taken from [12].
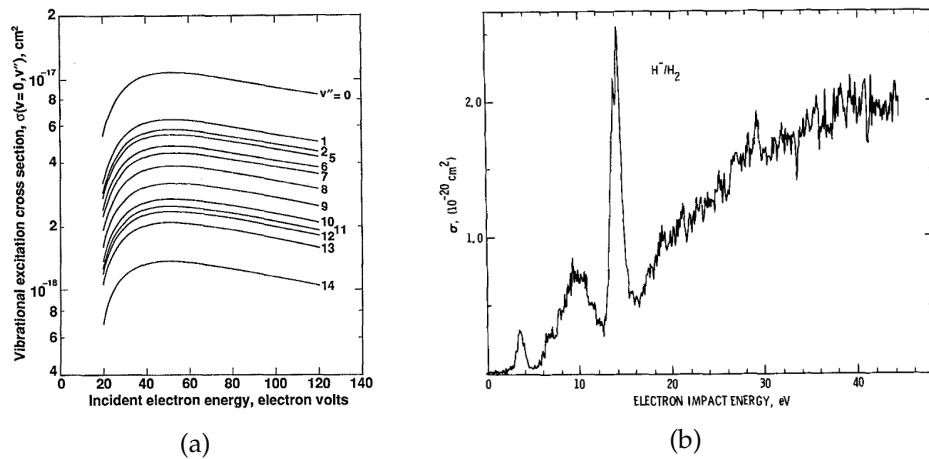

(a)   (b)

Figure 2.3: **(a)** Cross-section for vibrational excitation of the H_2 molecules as a function of the electrons energy. The picture is taken from [13]. **(b)** Total cross-section of the H^- production, including both the DEA and the polar dissociation. the monotonic increase after 17 eV is due to the fact that the polar dissociation of H_2 kicks in. The picture is taken from [14].
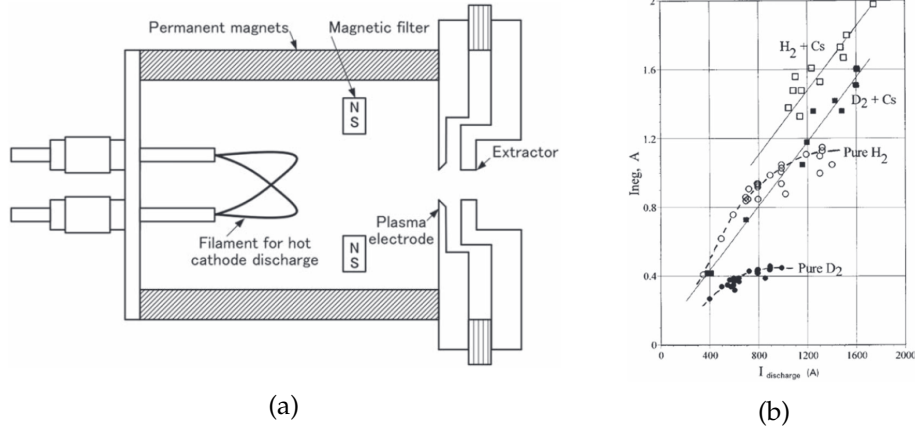
(a)

(b)

Figure 2.4: **(a)** Schematic illustration of the volume plasma negative ion source. The picture is taken from [6]. **(b)** Output current of a volume plasma source as a function of the discharge current. The addition of Cs vapor clearly enhances the output current. The picture is taken from [15].

- Addition of Cs vapor can massively enhance the D^- production (Fig. 2.4b) through charge exchange (Eq. 2.6), surface processes on the discharge electrodes, and also adding more electrons to the plasma due to their small ionization energy 3.9 eV.

2.2 Surface Sources

Apart from the volume processes, negative ions can also be formed on metallic surfaces where atom and the surface come into interaction [6, 16, 17]. This can happen, for example, through adsorption on the surface. To extract these negative ions from the surface, they need to gain momentum which can be provided through sputtering [18]. Negative ions can also be formed through the reflection of energetic atoms and positive ions off the surface where they can trap a freely wandering electron on the surface to their affinity level [19, 20, 21]. There has been quantum mechanical calculations for such a surface electron transfer process [17]. In the reflection process, the negative ion fraction β^- of the particles leaving the surface is calculated to be:

$$\beta^- = \frac{2}{\pi} \exp\left(-\pi \frac{\Phi - \mathrm{EA}}{2av_z}\right) \tag{2.7}$$

where Φ is the surface work function, EA is the electron affinity of the reflecting atom, a is an exponential decay constant, and v_z is the normal leaving velocity of the created ion off the surface. This familiar thermodynamical-like expression is easy to interpret. It states that there are two competing probabilities for the surface electrons: either the electron continues to stay

in the metallic surface state, or it moves to the affinity level of the reflecting atom. Basically, the higher the electron affinity, and the lower the work function, the more probable the negative ion production would be. Therefore, using the right surface with a low work function is very important. Surfaces of the refractory metals (e. g., W, Mo, Ta) with a sub-monolayer deposition of alkali metals (like Cs) have the lowest work function among surfaces. Hence they are massively used in different negative ion sources [6]. The other determining factor is the velocity. This is because the velocity determines the interaction time between the atom and the surface electric field[2]. The interaction with the surface electric field provides the environment for the leaving negative ion to lose its electron. Hence the higher the velocity the more negative ions would survive. Finally, The constant *a* depends on the atom species and the surface material [22]. Based on what has been discussed so far, surface sources of D$^-$ ion production can be divided to three types: sputtering sources, surface reflection sources, and finally surface plasma sources.

2.2.1 Sputtering Sources

These sources rely on the sputtering process to provide the momentum for the D$^-$ ions. The most versatile sputtering sources have been implemented with Cs$^+$ as the sputtering ion. Hence these sources are known in the literature and market as Cs sputtering sources. As displayed in Fig. 2.5, a Cs dispenser evaporates Cs into the space in between a hot tungsten ionizer and the target. As the Cs atoms hit the tungsten ionizer they are ionized and accelerated by the positive bias of the tungsten ionizer (anode) towards the negatively biased target (cathode). This create a local plasma which leads to the sputtering of the target by Cs$^+$ ions. Deuterium atoms can be supplied to the target surface through adsorption or the target material. The highest D$^-$ currents are produced with the latter approach where a target of compressed titanium deuteride TiD$_2$ powder is used [23]. This approach also has the advantage that the whole system is kept in UHV which makes it much easier to connect the negative ion production setup to ion trapping chambers or other systems which require UHV environments. The Cs$^+$ ions hitting the target surface releases deuterium atoms from the TiD$_2$ crystal. The released deuterium atoms can then pick a surface electron and leave the surface with the momentum transferred to them by the Cs$^+$ ions impact. It is worthy of noting that Ne$^+$ ions have also been investigated as the sputtering ion [18]. The choice of Cs$^+$ as the sputtering ion is motivated by the fact that some of the Cs vapor deposits on the target surface. Cs deposition on the surface decreases the work function which as discussed earlier enhances the negative ion production.

---

[2]I. e., the work function induced electric field at the surface.
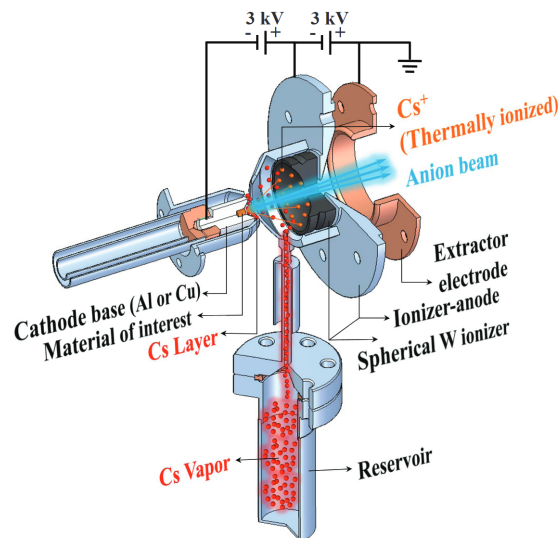
Figure 2.5: Schematic illustration of a Cs sputtering negative ion source. The picture is taken from [24].

2.2.2 Surface Reflection Sources

High currents of D^- have also been produced through the reflection of energetic deuterium positive ions [20, 21] and deuterium atoms (hot atoms) [19]. In the first approach a beam of D^+ ions is produced through hot filament discharge. These ions are then accelerated to $\sim$ keV energies, and then shot at the target. The target can be made of any type of metals; however, the usual choices have been alkali metals or refractory metals. See Fig. 2.6 for more details. The second approach, that is, the hot deuterium approach is much less efficient. In this approach, first, a super hot gas of atomic deuterium ($\sim$ 2500 K) is produced by passing the deuterium gas through a hot tungsten tube. Then, these super hot atoms effuse to the production chamber where they come into contact with the target, and a small fraction of them are back-scattered as D^- ions. Of course, Cs vapor can be added to the system in both approaches so that the work function of the target decreases, and more negative ions be produced.

2.2.3 Surface Plasma Sources

Further studies on volume plasma sources showed that the H^-, and D^- ion production depend on the filaments surface area [25]. This finding hinted at the presence of surface mechanisms in a volume plasma source. As a result, volume plasma sources have been modified to enhance the surface production. Fig. 2.7 shows how one example of a surface plasma source operates.
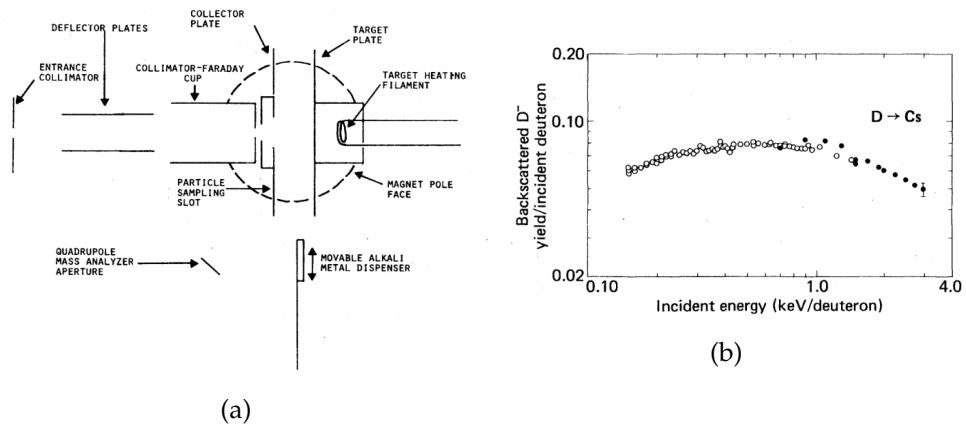
Figure 2.6: **(a)** Schematic illustration of a surface reflection negative ion source. H⁻ or D⁻ ions enter the apparatus from the "Entrance Collimator", then shot at the target. The picture is taken from [20]. **(b)** Back-scattered D⁻ yield vs incident energy for D_2^+ (filled circles) and D_3^+ (open circles) incident on thick Cs adlayer. The picture is taken from [20].

In this example the two hot filaments create the deuterium gas discharge plasma. The array of the magnets around the chamber are for the confinement and enhancement of the plasma as discussed for the volume plasma sources. The only added element here is the negatively biased "converter" electrode which has a large surface area. Therefore, more deuterium atoms adsorb and negatively ionize on this electrode surface. Bombardment of the electrode by the D⁺ ions then can sputter the surface-created D⁻ ions. The bombarding positive ions can also back-scatter as negative ions. To extract the negative ions and make the sputtering happen, the converter electrode is negatively biased to several hundreds of volt with respect to the plasma. Finally, Cs vapor can also be adder to this type of source to further enhance the D⁻ production.

Fig. 2.8 summarizes the main points that have been discussed so far on the D⁻ ion formation.

2.3 Pulsed Laser Negative Ion Source

First of all, using pulsed laser to produce negative ions is not a well-known technique, and still needs more research on different materials. Hence it can not yet be categorized as a surface or volume source type.

Nevertheless, pulsed lasers have been used to make positive ions [27], and this is a well-established method to create positive ions. To do so, one needs to prepare a clean solid target out of the desired material (e. g., Ag, Ta,
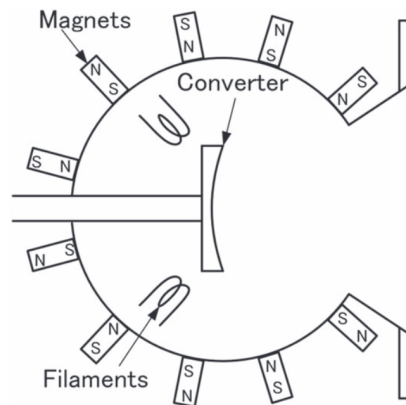
Figure 2.7: Schematic illustration of a surface plasma negative ion source. The collisions of the plasma constituents with the "Converter" electrode surface results in the massive enhancement of the negative ion production. The picture is taken from [26].
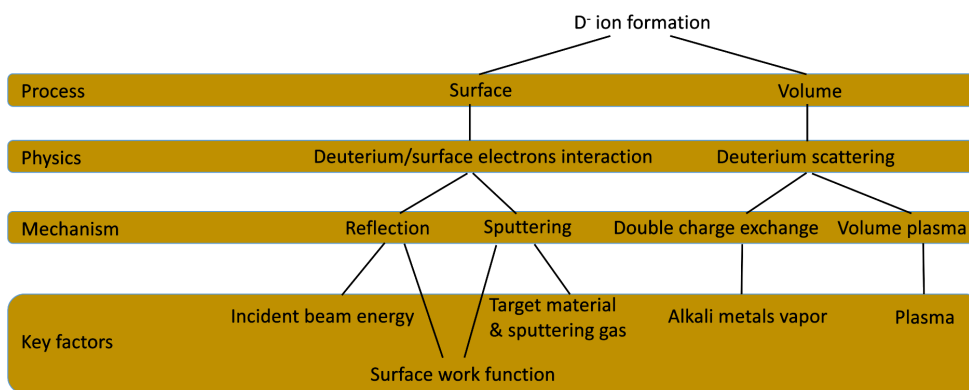

Figure 2.8: Summary of the D^- ion formation processes.

etc.), and irradiate it with a high power pulsed laser[3]. The highly focused energy of the laser pulses (> 1 mJ) instantaneously evaporates and sputters particles from the target creating a plasma plume in front of the target. This hot plasma consists of neutral atoms, clusters, ions, and electrons, and undergoes an adiabatic expansion as it is formed. According to [28], due to the smaller mass of the electrons they pick up higher momentum; therefore, they expand faster in space. This expansion creates a separation in between the electrons and the positive ions, hence creates a strong electric field which further accelerates the positive ions which results in the formation of highly energetic and broadly distributed positive ions (from 0 to MeV).

---

[3]To prevent the target surface from degrading and also to have a cleaner beam of positive ions it is preferred that the system operates under UHV.
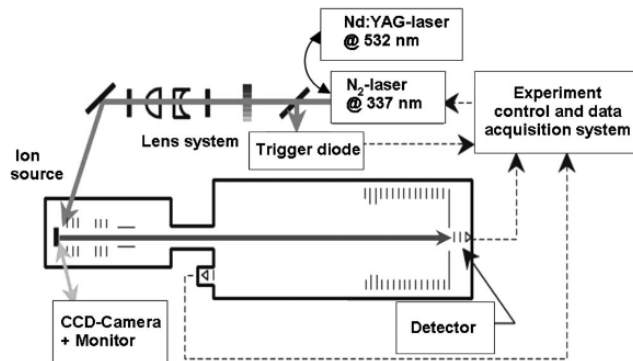
Figure 2.9: Schematic illustration of a pulsed laser negative ion source. The picture is taken from [29].

Apart from [29], where production of osmium negative ions using pulsed laser is reported, no other successful report in the literature was found up to our knowledge. The target they used was a pure solid osmium target. They found that for laser pulses above 500 μJ osmium negative ions can be produced, and the more the pulse energy, the more negative ions were created. It is also worthy of noting that the target material is crucial in producing osmium negative ions as they were not able to detect any atomic osmium negative ions with a target made of dried osmium solution $(NH_4)_2OsCl_6$. Fig. 2.9 shows the schematic illustration of their setup.

Pulsed laser approach can be investigated for the production of D⁻ ions too. In regards to the target choice, the first choice can be TiD_2 as it is the successfully tested target for the sputtering source.

In the next chapter the experimental setup for the D⁻ ion production in this project will be described. The experimental results will also be presented, and based on the results will be discussed what the dominant D⁻ ion production process in the setup is.

Chapter 3

Setup, Results, and Discussion

3.1 Setup

The design of the system is based on two vacuum chambers which are connected by a differential pumping constriction. One is the chamber to produce D^- ions which we refer to as the preparation chamber, and the other chamber is for ion trapping referred to as the trap chamber in this thesis. Since the trap chamber needs to be under UHV, a pressure difference has to be maintained between the trap chamber and the preparation chamber through a differential pumping constriction. A detailed description of the constriction as well as other components of the setup can be found in Matteo Simoni's master's thesis [30]. To maintain higher pressure differences the constriction needs to be longer or narrower, which makes it more difficult for the ions to pass through. Hence there is a trade-off between the pressure difference and the proportion of ions passing through the constriction. To produce D^- ions, a supply of deuterium is needed. In this setup the supply is provided by D_2 gas. The preparation chamber is filled with deuterium gas through a leak valve which connects the chamber to a deuterium bottle. Since we are able to produce D^- ions with pressures of the order of 10^{-6} mbar, we decided to keep the pressure in the preparation chamber below 10^{-5} mbar. This resulted in a constriction of a length of 3 mm and diameter of 1.5 mm. The schematic illustration of the system is shown in Fig. 3.1. To create D^- ions, the idea is that an electron gun (e-gun) shoots electrons at a tungsten grid[1,2]. The created D^- ions are accelerated by a negative pulse applied to the grid. Before the grid negative pulse, a short positive pulse is applied to the grid to attract the created ions closer to the grid so that the ions are more bunched-up. The accelerated ions go through an electrostatic (einzel) lens and two pairs of deflection plates which guide the ions into

---

[1]The grid consists of 50×50 tungsten wires in 1×1 inch with a wire width of 50 μm.

[2]In Sec. 3.4 I will discuss how the D^- ions are created in this setup.
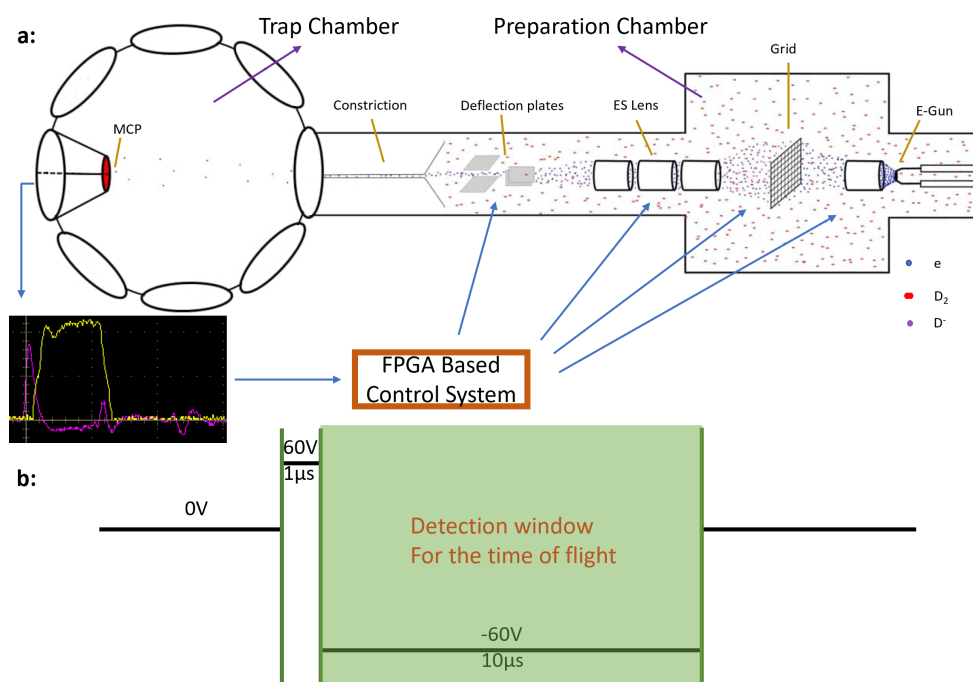
Figure 3.1: **(a)** Schematic illustration of the project setup. The D$^-$ ions are created, accelerated, and focused in the preparation chamber. The preparation chamber and the tarp chamber are connected by the differential pumping constriction to keep the pressure difference. On the bottom left it is shown how the MCP pulses look like (the purple pulse). These pulses are standardized by a discriminator board (the yellow pulse) and counted by the control system. The control system also produces signals to control the grid voltage, etc. **(b)** The time of flight (TOF) experimental sequence. A short positive 1 μs pulse is applied to the grid to attract the negative ions. This pulse is followed by a negative 10 μs pulse that accelerates the ions towards the MCP. The TOF is measured form the falling edge of the negative pulse. The magnitude and lengths of the pulses are studied in Chap. 3.

the constriction so that the ions reach the trap chamber. To detect the D$^-$ ions, a Z-stack microchannel plate (MCP) is used which produces electric pulses as the charged particles hit it. These pulses are then standardized by a discriminator board and counted by the control system (See Chap. 4.) The control system also produces signals to control the grid voltage, deflection plates, etc.

To investigate what ions are produced, time of flight (TOF) spectroscopy needed to be done. At first, TOF experiments were done in the preparation chamber. Afterwards, the preparation chamber was connected to the trap chamber [30], and TOF experiments were done again to see if any ions pass-
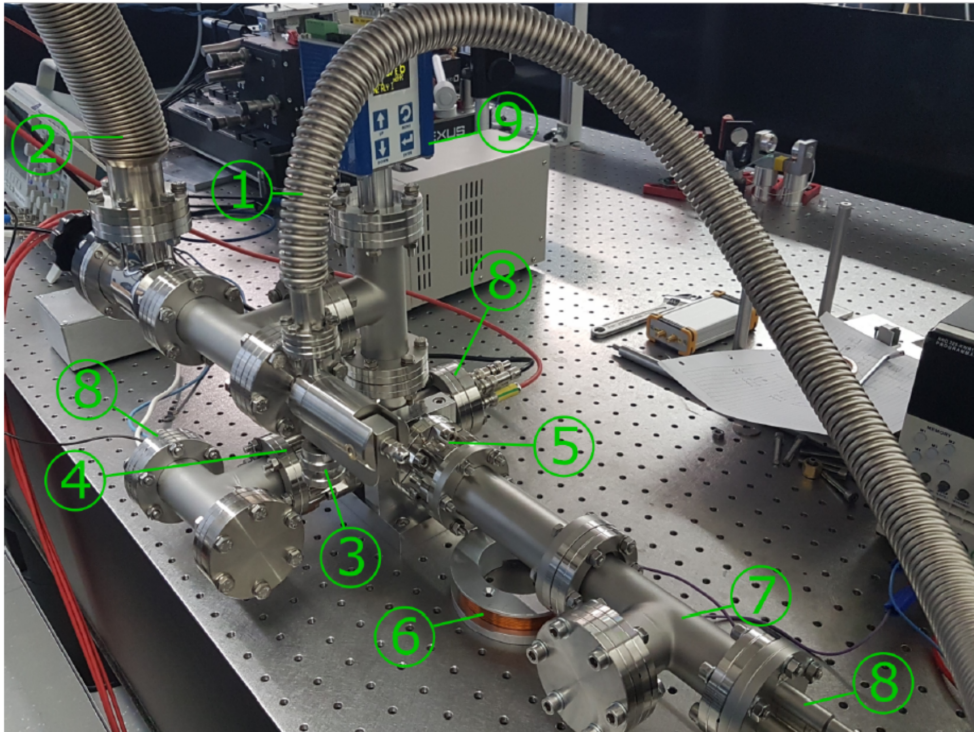
Figure 3.2: Picture of the preparation chamber taken from [31]. We have: 1) the tube connecting to a D_2 bottle; 2) the tube connecting to a turbo pump; 3) the leak valve to control the flow of D_2 molecules into the chamber; 4) the e-gun; 5) the tungsten grid to accelerate the particle, and the electrostatic lens; 6) a coil to deflect the electrons; 7) the MCP; 8) the MCP feedthroughs; 9) a pressure gauge.

ing through the differential pumping constriction can be detected. In what follows, the data collected for the preparation chamber is discussed, then the data for the connected chambers.

3.2 TOF in the Preparation Chamber

The purpose of doing TOF experiments in the preparation chamber was first, to compare the results with the results presented in Silvan Koch's master's thesis[3] [31], and secondly, to make adjustments to the contributing factors to enhance the ion production. Fig. 3.2 illustrates how the setup looked like at the beginning. The comparison of the results with the results in [31] was necessary because the data presented in this thesis are collected by use

---

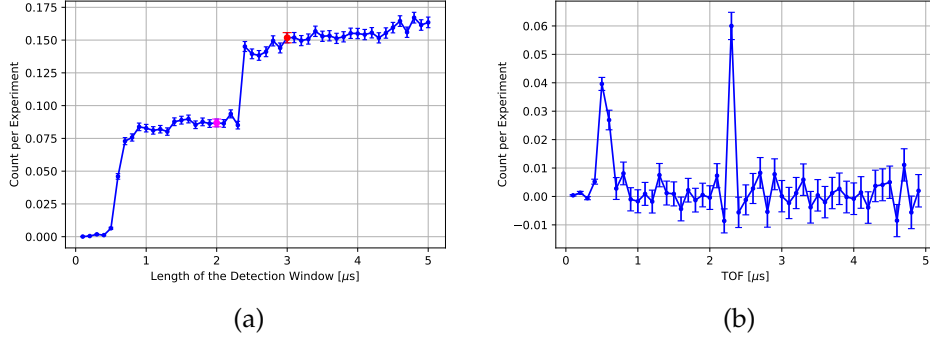[3]Silvan had been the master's student working on this project before Matteo Simoni and I.

Figure 3.3: **(a)** Example of the TOF signal. The first and the second steps are due to the arrival of electrons, and H⁻ ions. The magenta point shows that when the detection window is kept open for 2 μs (3 μs), we measure 0.085 (0.15) counts per experiment, i. e., per grid negative pulse. **(b)** Example of the initial analysis performed on the data of **(a)** in order to find the TOF of the registered counts.

of an FPGA based control system[4] while, before, a gated counter and delay generator was being used to do so. During the time that we were studying the TOF in the preparation chamber, the control system was programmed to produce a cumulative TOF data. Fig. 3.3a shows how a typical result of the TOF signal looked like. This plot shows the cumulative TOF, meaning that each point denotes the total number of particles detected within the time denoted on the horizontal axis. This time is measured from the falling edge of the grid negative pulse. Fig. 3.3b is derived from the cumulative TOF data by finding the difference between each two points in the cumulative data. Therefore, this plot shows only the registered counts within the TOF time step which was set to 100 ns there.

A coil was used (Fig. 3.2) to create a magnetic field on the path of the accelerated particles. When using the coil, the first step in Fig. 3.3a gets suppressed while the second step remains unchanged. Hence we conclude that the first peak represents electrons and the second peak some heavier charged particles. Based on the acceleration pulse (i. e., the grid negative pulse), we applied a current of 5 A to 11.9 A to the electromagnet coil. The coil produces a magnetic flux of roughly 5 G at the center of the tube at 5 A. If electrons are accelerated under a voltage V, then the radius of their cyclotron movement in the magnetic field is:

$$r_e = 3.36 \frac{\sqrt{V}}{B} \text{ [cm]}. \tag{3.1}$$

---

[4]FPGA stands for field-programmable gate array. The control system is used to count the detection pulses from the MCP.
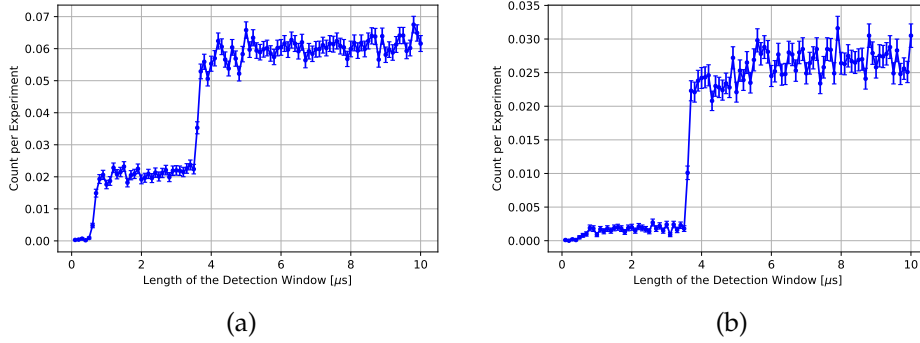
Figure 3.4: **(a)** TOF signal in the preparation chamber with $V_{neg} = 60$ V, $I_{emission} = 10$ μA, $I_{coil} = 5$ A. **(b)** Repetition of **(a)** with $I_{coil} = 11$ A.

From the Biot-Savart law, we know that the magnetic field scales linearly with the current. We also know that the particles are accelerated under the grid negative pulse. Hence to keep the radius of curvature of the charged particles constant for different grid pulses, we kept $\sqrt{V_{neg}}/I_{coil}$ constant. Fig. 3.4 shows the difference when a current of 5 A or 11 A is applied to the coil when $V_{neg} = 60$ V. By looking at the radii of different charged particles we can see why only the step attributed to the electrons is suppressed.

$I_{coil} = 5$ A:

$r_e \approx 0.7\sqrt{60}$ cm ≈ 5.2 cm

$r_{H^-} = \sqrt{\frac{M_{H^-}}{M_e}} r_e \approx 42 r_e \approx 218$ cm

$r_{D^-} = \sqrt{\frac{M_{D^-}}{M_e}} r_e \approx 60 r_e \approx 311$ cm

$I_{coil} = 11$ A:

$r_e \approx 5.2\frac{5\,\text{A}}{11\,\text{A}}$ cm ≈ 2.4 cm

$r_{H^-} \approx 42 r_e \approx 99$ cm

$r_{D^-} \approx 60 r_e \approx 141$ cm

The distance between the coil and the MCP is about 5 cm, so when the current is set to 11 A all the electrons are deflected from the MCP. For the ions the cyclotron radius is too large to affect the detection.

Two aspects of the TOF data can be looked at: the magnitude of the peaks, and the timing of the peaks. Using the timing of the peaks mass spectroscopy can be done. Analysing the magnitude of the peaks helps adjust the beam optics and the grid pulses so that maximum negative ion count-rate is obtained.

3.2.1 Mass Spectroscopy

To find the mass of the heavier charged particles that the second step represents, we changed the grid negative pulse from 60 V to 460 V in steps of 50 V, and plotted the TOF versus the grid negative pulse. If we ignore the time that the ion needs for acceleration until it reaches its final velocity, and also we ignore the time of switching to the grid negative pulse, we expect the TOF to be:

$$v = \sqrt{\frac{2qV_{neg}}{m}} \qquad (3.2)$$

$$\text{TOF} = \frac{L}{v} = L\sqrt{\frac{m}{2qV_{neg}}}. \qquad (3.3)$$

If we substitute $L = 27$ cm and $m = M_e$ and $q = Q_e$, we see that the TOF is approximately 60 ns for $V_{neg} = 60$ V and 22 ns for $V_{neg} = 460$ V. Since our time resolution in these experiments is 100 ns, we can say that the TOF of electrons is approximately zero. However, we see a non-zero TOF for the first step in the TOF plot in Fig. 3.3a. This non-zero time is caused by delays consisting of "control delay" plus "detection delay". Control delay is the delay between the time that the control system produces the control pulse to switch the grid voltage and the time that the grid physically switches. Detection delay is the delay between the time that a detection pulse is created in the MCP and the time that the control system registers this pulse. Assuming that the first step represents electrons, and ignoring their TOF in comparison with lightest negative ions[5], the position of the first step can be used as a calibration of the overall delay and is subtracted from the TOF data for the second step. By analysing the TOF data, we find that depending on the grid negative pulse the electron TOF is between 550 ns to 400 ns. After subtracting this from the heavier charged particles TOF, we see that the heavier charged particle fits neither H^- nor D^- ion (Fig. 3.5).

The problem lies in us neglecting the effect of grid switching. Eq. 3.3 is only valid if the switching from grid positive pulse to grid negative pulse takes place instantaneously; however, in reality there is a switching time involved. To measure the grid voltage, a 1 GHz 10x probe and a 5 GHz sampling rate oscilloscope were used. The probe was directly connected to the SHV cable coming out of the high voltage switch. Hence in this measurement the possible effects of the grid on the switch voltage are ignored. Fig. 3.6 shows how the "grid voltage" looks like during a pulse sequence in reality. This non-zero switching time results in ions accelerating before the grid reaches

---

[5]Since the hydrogen mass is roughly 1836 times the electron mass, the H^- and D^- ions TOFs are roughly 43 and 61 times the TOF of electrons. Hence the electrons TOF is ignored in the calculations in this thesis.
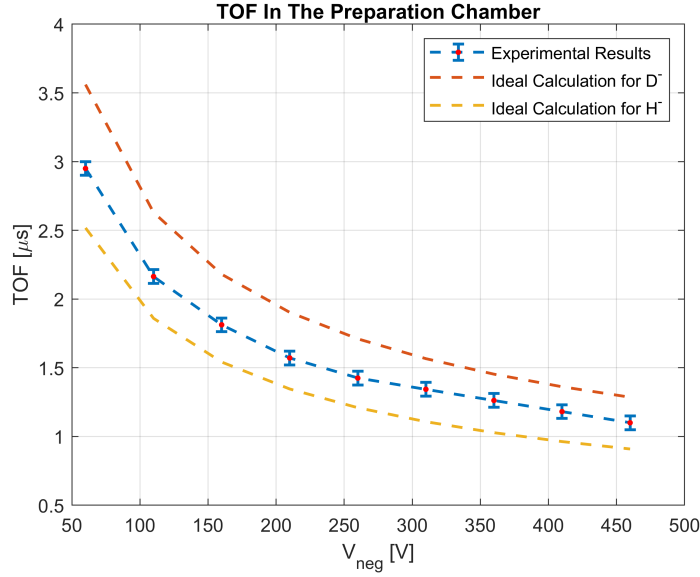
Figure 3.5: Comparison of the experimental TOF data with the ideal calculation in Eq. 3.3 for the heavier particle peak.

the set V_{neg}. Consequently, the ions experience a lower acceleration, and end up having a larger TOF than the ideal case. To have a more accurate calculation of the TOF, I did a Comsol simulation of the potential landscape inside the chamber taking into account the grid and the lens voltages (Fig. 3.7). Then, I used this potential landscape together with the oscilloscope data on the switching behavior of the grid, and solved the time dependent Newton equation for electrons, H^- and D^- ions. A total number of 500 particles evenly axially distributed[6] over 300 μm of the grid (on both sides) were simulated. Fig. 3.8a shows the result of the simulation alongside the experimental data. This plot shows that the charged particles fit the H^- ion simulation within their error bar. The error for the charged particles is considered to be 50 ns because of the 100 ns time resolution in the TOF data. For the simulation the error is considered to be 10 ns because of the uncertainty in the switching time. To measure how well the simulation and the experimental data compare, reduced chi-squared is calculated:

$$\chi_{red}^2 = \frac{1}{n} \sum_{i=1}^{n} \frac{(O_i - C_i)^2}{\sigma_i^2} \tag{3.4}$$

where O_i is the experimental TOF, C_i is the simulated TOF, and σ_i^2 is the summation of the simulation (10^2 ns^2) and experiment (50^2 ns^2) error variances. Finally, the reduced chi-squared is calculated to be $\chi_{red}^2 = 1.38$. It is

---

[6]This means that the simulation is one-dimensional.

close to unity; hence it can be concluded that the detected charged particles are H$^-$ ions. This is an interesting result, because the preparation chamber is filled with 2×10^{-6} mbar of D$_2$ molecules, so there should be no comparable amount of hydrogen gas inside the chamber[7]. Nevertheless, since the grid and the whole chamber were exposed to air before going to high vacuum conditions, water molecules adsorb on the grid as well as the surfaces of the chamber[8]. For example, for stainless steel, as depicted in Fig. 3.8b, typically a 10-20 nm oxide layer is formed on the surface. On top of this layer there is a monolayer of chemically adsorbed water, and then there are multiple layers of physically adsorbed water on the top. The water adsorption on metallic surfaces is a dissociative process in which water molecules dissociate into adsorbed OH molecules, H and O atoms [32, 33, 34, 35]. It is possible that the adsorbed water is the main source of hydrogen in our system. This theory could also explain the constant drop in the H$^-$ count-rate [30]. The drop in the count-rate means that when we turn on the e-gun, and produce H$^-$ ions we lose some of the hydrogen and the hydrogen supply partially depletes. The decrease of the H$^-$ count-rate, however, slows down quickly after a few hours. It could be that the depletion is countered by the constant outgassing of water from the chamber walls. The outgassed water molecules can adsorb on the grid and replenishes the hydrogen source.

With the right conditions, we could also see a small bump in the TOF plot (Fig. 3.9a). Right conditions mean higher V_{neg}, $V_{lens}/V_{neg} \approx 0.5$ and small background electrons (i. e. $r_e \leq 5$ cm). However, due to insufficient statistics the signal is so small that it can not be used for mass spectroscopy. Nevertheless, based on the further evidence that we observe in the TOF after connecting the two chambers, we can conclude that this signal represents D$^-$ ions.

3.2.2 Source Optimization

We also investigated the effect of e-gun bias and Wehnelt voltages (V_{bias}, $V_{Wehnelt}$), the lens voltage (V_{lens}), and the grid pulses ($V_{pos}, t_{pos}, V_{neg}, t_{neg}$) in order to maximize the negative ion production.

E-Gun

We investigated the effect of V_{bias} (the electron energy) in H$^-$ production and we found that up to 30 eV the production monotonically increases with

---

[7]There is, however, one small source of hydrogen outgassing inside the vacuum chamber. This outgassing is caused by hydrogen diffusion in the stainless steel. This hydrogen outgassing is only relevant in UHV conditions and also depletes over years, and can not be recharged by venting the chamber with air. Hence this source of hydrogen can be neglected.
[8]This results in adsorbed water to be the main source of outgassing in high vacuum.
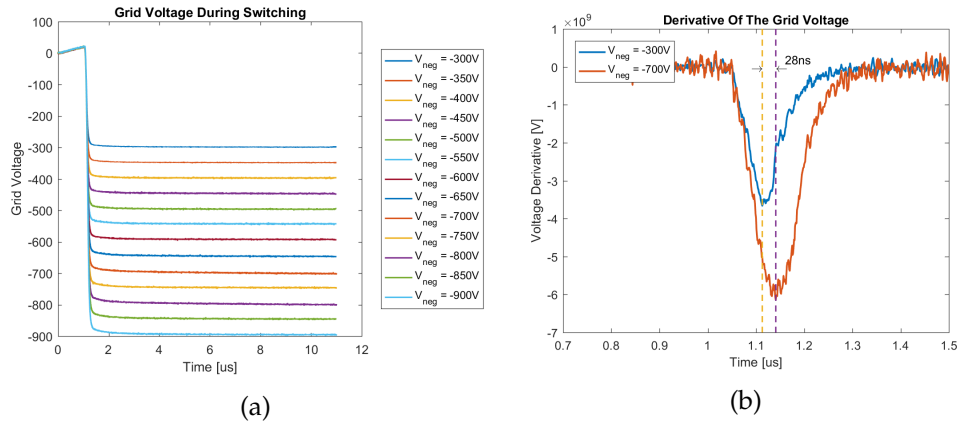
(a)

(b)

Figure 3.6: **(a)** "Grid voltage" during each TOF experiment for different grid negative pulses. $V_{pos} = 60$ V for all the cases. It can be seen that the "grid voltage" does not reach the set value for the positive pulse, and there is also some non-zero switching time for both positive and negative pulses. **(b)** The derivative of the "grid voltage" shown in **(a)** for $V_{neg} = 300, 700$ V. The switching takes more time as the negative pulse is increased.
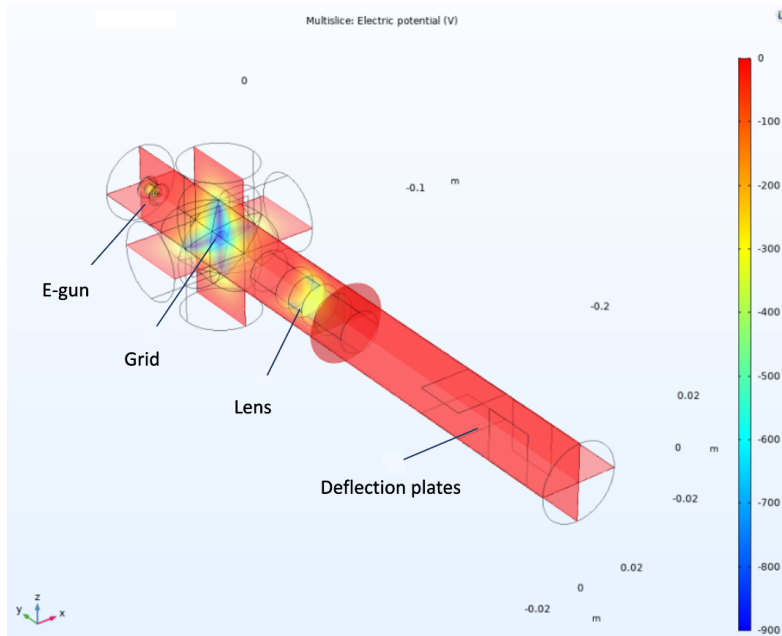

Figure 3.7: Comsol simulation of the chamber to find the potential landscape. The potential landscape is used for the TOF simulation.
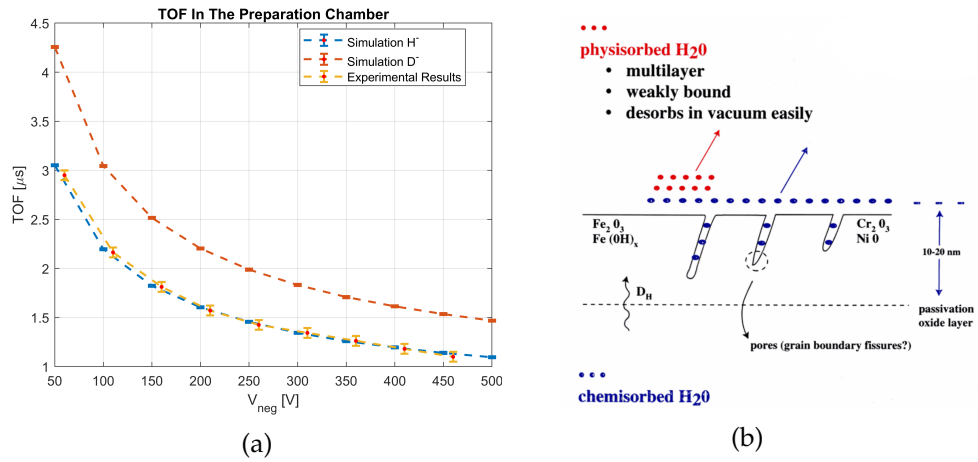
(a)   (b)

Figure 3.8: **(a)** Comparison between the TOF results in the preparation chamber and the simulation. The reduced chi-squared χ^2_{red} is calculated to be 1.38 for the fit to the simulation for H^-. **(b)** Water adsorption on stainless steel in high vacuum. There is a couple of nm of oxide layer, a monolayer of chemisorbed water, and multilayer of physisorbed water on the stainless steel surface. The picture is taken from [35].
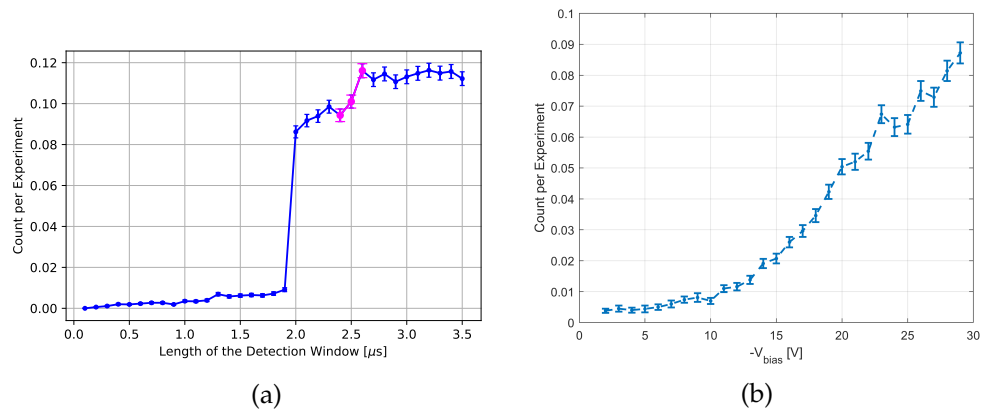

(a)   (b)

Figure 3.9: **(a)** Demonstration of the small bump in the TOF signal after the H^- peak. **(b)** Experimental results on the effect of electron energy, i. e. e-gun bias voltage. Unlike the DEA cross-section we see a monotonic increase in the H^- production with the electron energy.
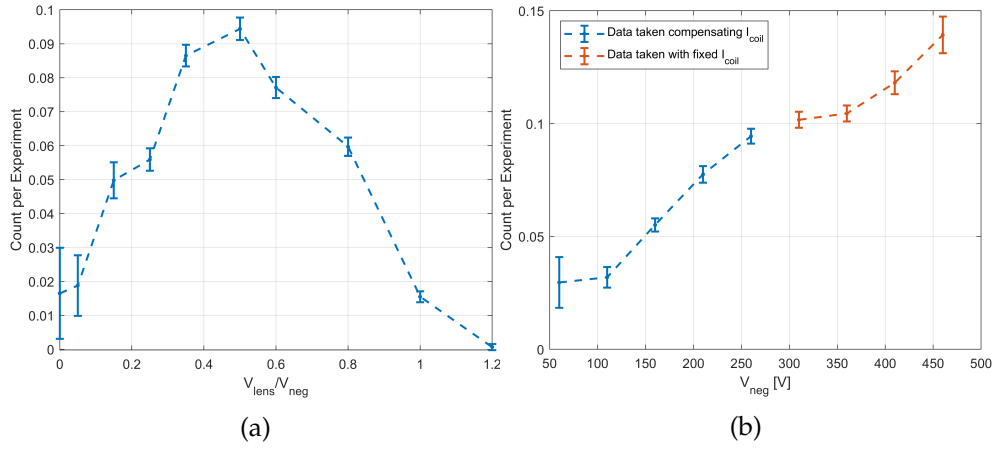
Figure 3.10: **(a)** H^- ion count-rate as a function of V_{lens}/V_{neg}, the ratio between the einzel lens voltage and the grid negative voltage for the case in which $V_{neg} = 260$ V. **(b)** H^- ion count-rate as a function of the grid negative voltage V_{neg}. The data in blue have been collected by changing I_{coil} to maintain the cyclotron radius fixed as V_{neg} was increased; for the data in red it was not possible to keep the radius fixed due to the limitation in the coil current.

electron energy (Fig. 3.9b). To have a similar focusing behavior from the e-gun we kept the ratio of $V_{Wehnelt}/V_{bias}$ constant at 1.05, and also the emission current was kept at 10 μA.

Lens

To focus the charged particles at a certain point the ratio of V_{lens}/V_{neg} matters. We found this ration to be 0.5 (Fig. 3.10a) to maximize the detection of particles by the MCP. Nevertheless, this 0.5 ratio is not important anymore now. Because the setup has changed, and the lens now should focus the ions into the constriction. However, this result is important in the sense that shows the effectiveness of the lens.

Grid Pulse Sequence

We did not study the effect of the magnitude of the positive pulse in detail. In all the experiments presented throughout this thesis the positive pulse is 60 V and 1 μs. Nevertheless, in reality the grid voltage never reaches its set positive value. For example, if we set the positive pulse to 60 V the grid voltage only reaches 20 V in 1 μs (Fig. 3.6).

We observed that H^- count increases monotonically with the positive pulse voltage from 0 V to 100 V by a factor of less than 2; the effect was not studied further. On the other hand, increasing the positive pulse length caused the

TOF signal to be spread out instead of being peaked at a certain time. We assume that the charged particles undergo an oscillatory motion around the grid when a positive voltage is applied to the grid. Hence longer grid positive pulses broaden the velocity distribution of electrons and negative ions. This is not desirable for ion trapping, because we need the negative ions to be bunched up, and arrive at the same time at the trap[9].

The ion count also increased with increasing the negative pulse voltage (Fig. 3.10b). We assume that the monotonic increase in the count-rate as the negative voltage increases is caused by more efficient collection of the negative ions around the grid. The pulse must be longer than the negative ions TOF so that they do not get affected by changes in the grid potential. Apart from this, the pulse length does not matter. Hence we chose the pulse length to be 5 μs which is long enough to detect all the particles. For measurements done after connecting the two chambers we chose the pulse length to be 10 μs, because of the longer path of flight.

3.2.3   Comparison With the Former Results

In terms of the mass spectroscopy, contrary to our result, the negative ion peak is deduced to represent D^- ion in [31] (Fig. 3.11a)[10]. It is difficult to comment as to why there is this difference in conclusions between this work and the work presented in [31]. As mentioned in Sec. 3.2, change in the data acquisition is the only change in the setup in comparison with the past. The control system in the current setup has the advantage of a better time resolution (up to 4 ns) and higher data acquisition rate. There is also a difference in the data analysis. In this work a simulation is used to compare with the experimental data. However, in [31], Eq. 3.3 was used for to do so.

In relation to the source optimization, a different result for the e-gun bias is presented in [31]. Contrary to this work, two peaks are found in the ion production at $V_{bias} \approx -6\ V$ and $V_{bias} \approx -27\ V$ (Fig. 3.11b). It is not clear as to why there is such a difference in this measurement.

3.3   TOF After Connecting the Two Chambers

After connecting the preparation chamber to the trap chamber through the differential pumping constriction, no signal could be detected with the system settings obtained from the previous setup. In the effort to detect charged

---

[9]A spread of the order of 10 ns would be good desirable trapping. For more information on the trapping please refer to the forthcoming master's thesis of Georg Engin-Deniz.

[10]Here I am referring to the main peak not the bump. Silvan also used to sometimes observe a small bump after the negative ion peak, but due to lack of sufficient statistics he could not analyse its mass.
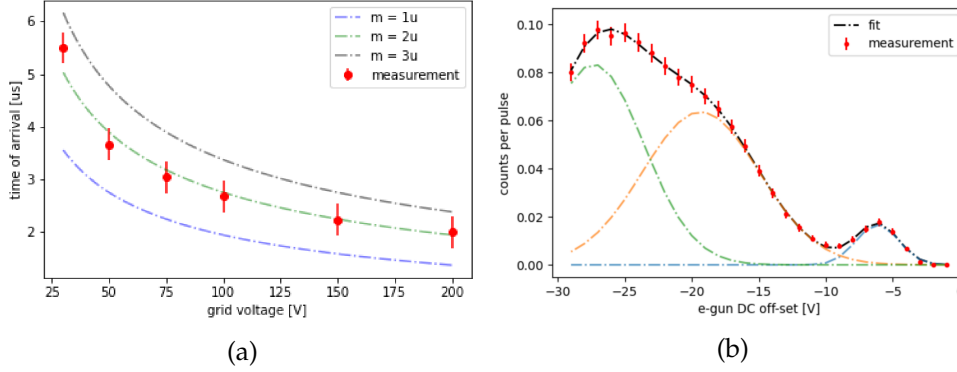
Figure 3.11: **(a)** TOF mass spectroscopy presented in [31]. Dashed lines represent predicted TOF for $m = 1u$, $2u$, $3u$ particles with charge $q = Q_e$. The lens to grid voltage ratio was kept constant at 0.75 to ensure there is no change in focal length. **(b)** The measured count-rate as function of the e-gun bias presented in [31]. The ratio of the Wehnelt cylinder voltage to the e-gun bias is kept constant at $V_{Wehnelt}/V_{bias} = 1.05$. The black dashed line is the sum of three Gaussians centered at -6.1 V, -19.3 V, and -27.3 V.

particles, we did not change the e-gun parameters, nor the grid positive pulse:

$$V_{bias} = -20 \text{ V}, V_{Wehnelt} = -21 \text{ V}, I_{emission} \approx 30 \text{ } \mu\text{A}, V_{pos} = 60 \text{ V}, t_{pos} = 1 \text{ } \mu\text{s}.$$

However, we changed the grid negative pulse V_{neg} (from 60 V to 260 V), the lens voltage V_{lens} (from -250 V to 0 V), and the deflection plates voltages (from -62 V to 62 V)[11] and we detected nothing.

It was Fig. 3.10b that help us make a breakthrough. This result suggested that we should expect to see an increase in the negative ion production with further increasing the grid negative pulse. Hence we set V_{neg} to 1000 V, and V_{lens} to zero, and did another voltage sweep in the deflection plates plane (Fig. 3.12a). Fig. 3.12a show two bright spots. The brighter one which is around $(V_L, V_T) = (40, -40)$ V is caused by electrons as we can get rid of it with applying a magnetic field. The fainter spot which is around $(V_L, V_T) = (15, 5)$ V is formed by negative ions.

3.3.1 Mass Spectroscopy

Fig. 3.13a shows the TOF result at the brightest point in Fig. 3.12b. We see two pronounced peaks around TOF = 2 μs. The first peak represents H$^-$ and the second one D$^-$. Over the time that we studied the system, we noticed

---

[11]At $V_{neg} = 260$ V this sweep in the deflection plates voltages results in probing a beam of a diameter of 0.6 cm.
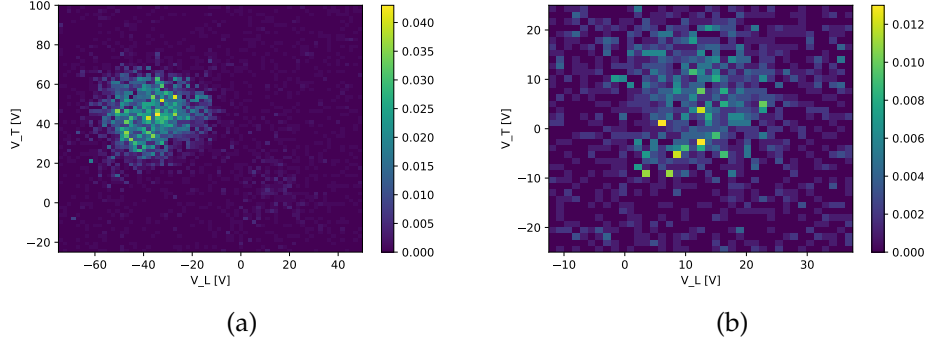
(a)

(b)

Figure 3.12: **(a)** 2-D voltage sweep of the deflection plates at $V_{neg} = 1000$ V, $V_{lens} = 0$ V, $V_{bias} = -20$ V, $I_{emission} = 32.9$ μA. V_T and V_L represent the top and the left deflection plates.The bottom and the right deflection plates are grounded. There are two spots detected in this test. A bright spot which represents the electrons, and a faint spot around $(V_L, V_T) = (15, 5)$ V representing heavier particles. **(b)** Zoomed into the heavier particle signal plotted in **(a)**. Pictures are taken from [30].
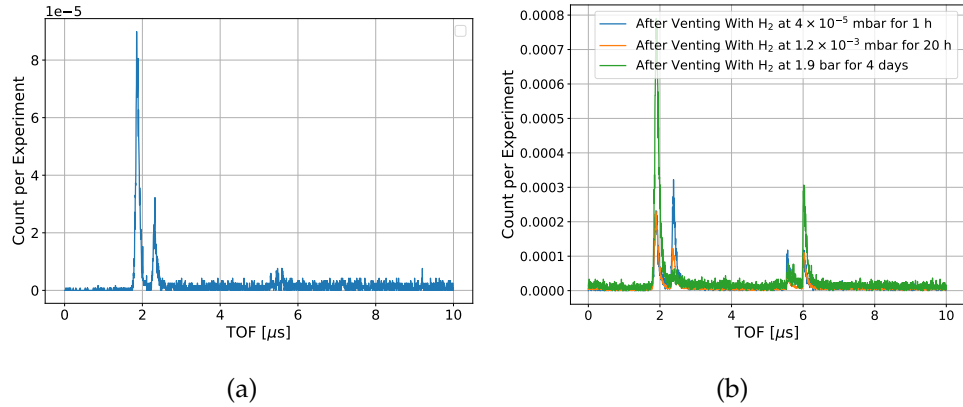

(a)

(b)

Figure 3.13: **(a)** The first TOF signal after connecting the two chambers. $V_{neg} = 1000$ V, $V_{lens} = 0$ V, $V_{bias} = -20$ V, $I_{emission} = 32.9$ μA. It is performed on the spot in Fig. 3.12b. **(b)** TOF signal after venting the preparation chamber with hydrogen. The blue, orange, and green TOF data are taken in chronological order. The first and fifth peaks increase, the second and forth peak diminish, and the third peak decreasing over time.

that three new peaks started to appear in the TOF signal. Fig. 3.13b shows the TOF signal roughly two months after the first result which is shown in Fig. 3.13a. The additional peaks are also present, but slightly shifted toward lower TOFs in Fig. 3.13a because of larger grid negative pulse (1000 V for Fig. 3.13a, and 900 V for Fig. 3.13b). The new peaks (peak 3 to 5) caught our attention when we managed to raise the count-rate through methods which are going to be discussed in Sec. 3.3.2. The result of the mass spectroscopy is shown in Fig. 3.14. Based on the simulation, the first to the forth peaks represent negative ions of a mass to charge ratio of 1 (H^-), 2 (D^-), 17, and 18 (Tab. 3.1). The simulation, and the reduced chi-squared calculation methods used here are the same as what has already been discussed in Sec. 3.2.1[12].

In addition to the simulation, replacing the D_2 gas with H_2 also suggests that the first peak represents H^- [30]. Fig. 3.13b shows three TOF measurements after venting the chamber with hydrogen. The surface adsorption of hydrogen is much less than water in high vacuum conditions. I assume that is why no change is observed in the peaks after filling the chamber with 4×10^{-5} mbar of hydrogen gas for 1 hour (the blue curve in Fig. 3.13b). No change is also observed in the first peak after raising the hydrogen pressure to 1.2×10^{-3} and staying there for 20 hours (the orange curve). However, it can already be seen that the second peak is diminished in comparison to the blue curve. Next, the chamber was filled with 1.9 bar of H_2 gas for 4 days. It is observed that the first peak tripled while the second peak totally diminished (the green curve in Fig. 3.13b). This could be explained by the supply of hydrogen increasing, and the supply of deuterium depleting. Higher hydrogen pressure could boost the surface supply of hydrogen in two ways: adsorption, and diffusion. From the Langmuir adsorption model:

$$\theta(p) = \frac{kp}{kp + k'}$$

where θ is the fractional occupancy of the adsorption sites, and p is the gas pressure, k is the adsorption rate, and k' is the desorption rate. This equation shows that higher pressure forces the adsorption to be higher. Higher hydrogen pressure also results in the diffusion of the hydrogen atoms into the surface of the grid [36]. Hence it boosts the hydrogen supply in the grid. Consequently, after keeping the chamber in 1.9 bar of hydrogen for 4 days the supply of hydrogen was increased while the supply of deuterium was depleted due to desorption and lack of replacement, because there was no deuterium inside the chamber anymore. Hence the results from this test strengthens the claim that the first peak represents H^- ion, and the second

---

[12]In these experiments the time resolution was 4 ns, so the negative ion TOF error is not limited to the time resolution but the uncertainty in the fit to the TOF peak. Hence to calculate σ_i^2 in Eq. 3.4, the fit uncertainty, and the electron TOF uncertainty (20 ns) and the simulation uncertainty (10 ns) are propagated: $\sigma_i^2 = \sigma_{i,fit}^2 + 20[ns]^2 + 10[ns]^2$. The electron TOF is measured to be 430 ± 20 ns.

peak represents D$^-$ ion. Regardless of the pressure that the chamber had been kept in during venting, all the TOF experiments were carried out at $\sim 10^{-6}$ mbar, like the rest of the TOF experiments presented throughout this thesis.

With the help of the simulation, and based on the existing elements inside the chamber, we can also deduce that the third and forth peaks represent OH$^-$ and OD$^-$, specially that the forth peak is always smaller than the third peak. This difference in the peak magnitude is expected based on two factors. One is the isotope effect between deuterium and hydrogen which results in deuterium having less tendency to be negatively ionized [6]. The other factor is that OH molecules are presumably already present on the grid as a result of water dissociative adsorption. The OD$^-$ ions are assumed to be formed on the grid surface from the water and deuterium dissociative adsorption which produce D and O atoms. These atoms might meet at the surface and form OD molecules. As to why the OD$^-$ peak did not fully diminish like the D$^-$ peak after venting the chamber with hydrogen, it can be argued that because of the strong bond between O and D the OD supply is more preserved than D. The fifth peak has a mass to charge ratio of $M/Q \approx 20$, but we can not think of any negative ions with such a mass to charge ratio.

Peak	Ion	χ^2_{red}
1	H$^-$	4.13
2	D$^-$	2.05
3	OH$^-$	0.68
4	OD$^-$	1.49

Table 3.1: Results of the TOF mass spectroscopy.

Fig. 3.13b also shows that after venting the chamber with 1.9 bar of hydrogen the fifth peak increases. The same thing happened when we replaced the H$_2$ bottle back with D$_2$ and vented the chamber with 2 bar of deuterium. These observations hint that this peak might be composed of a combination of deuterium and hydrogen. It could also be the result of some sort of contamination.

3.3.2 Source Optimization

Like the measurements done in the preparation chamber, we investigated the e-gun voltages V_{bias}, $V_{Wehnelt}$, the lens voltage V_{lens}, and the grid negative pulse V_{neg} in order to maximize the negative ion production.

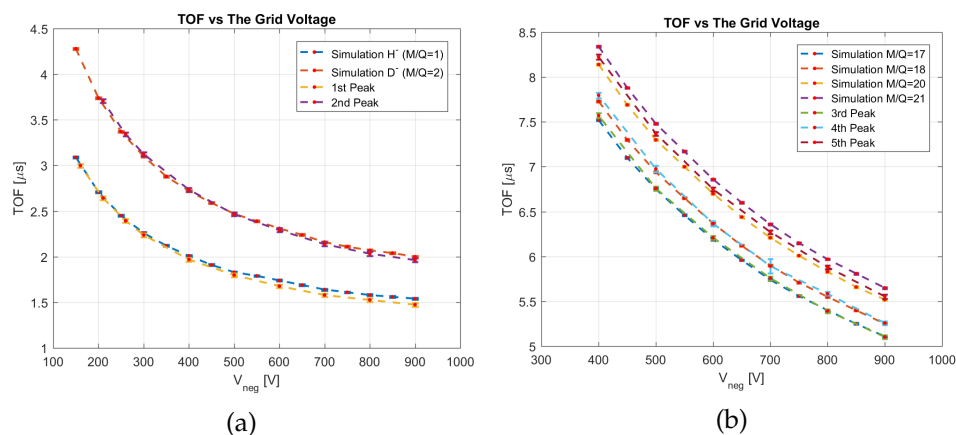Up until the last couple months of this thesis, the general consensus among

Figure 3.14: Comparison between the experimental TOF results and the simulation after connecting the two chambers for **(a)** the first and second peaks, and **(b)** the new peaks.

us was that the D^- ions were created in our setup through DEA. However, this belief gradually changed as we did more time of flight experiments, and found more evidences that pointed towards surface production. To more accurately investigate the D^- ion formation process in our setup, I proposed to make a couple of additions to our setup. One change was the addition of a new e-gun which enables us to have electrons of two different energies. With one e-gun set to a resonance in the DEA cross-section, and the other one set to the most efficient energy for vibrational excitation of D_2 molecules, I used the two e-guns to investigate the DEA theory in our setup. The other change was the addition of a Cs dispenser close to the grid which enables us to deposit a thin film of Cs on the grid, and investigate its impact on the D^- ion production.

In the following I will first go through the results for the e-gun, lens, and grid optimization; then, present the results after making the new additions.

E-Gun

We have seen already in Fig. 3.9b how the negative ion count changed with electron energy in the preparation chamber. One of the experiments that I did after connecting the two chambers was to go beyond 30 eV electron energy, and see what the effect is. I changed the electron energy from 20 eV to 430 eV and measured the count for different peaks in the TOF signal. Fig. 3.15a shows the result of this experiment. A massive boost in the negative ion production is obtained after increasing the electron energy. The first two peaks, H^- and D^-, increased by a factor of 100 from 20 eV to 192 eV. The other three peaks increased massively as well; however, due to lack of
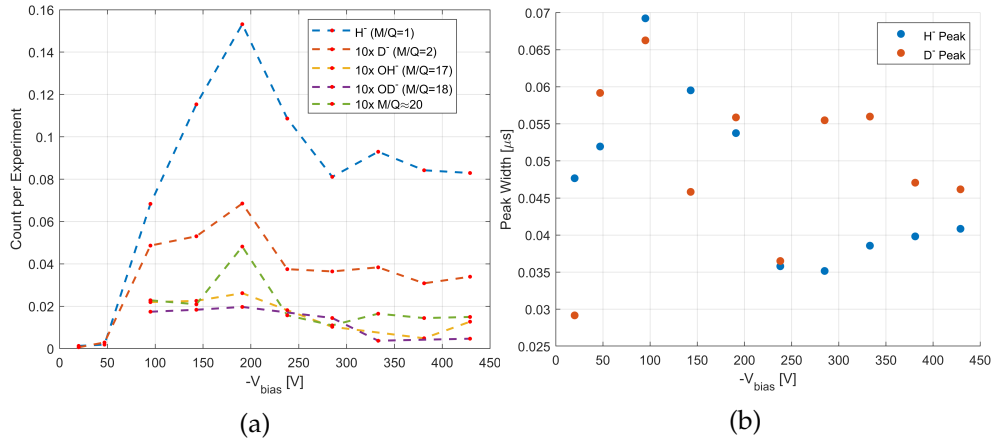
Figure 3.15: **(a)** Different negative ions count-rates as a function of electron energy. **(b)** The widths of the H^- and D^- peaks as a function of the electron energy.

sufficient statistics at 20 eV I could not calculate the boost. After 192 eV we observe that the counts dip, but this dip does not continue, and finally the counts stabilize. Fig. 3.15b shows the width of the H^- and D^- peaks as a function of the e-gun bias. We do not see a clear trend in the peaks widths, and it seems that the electron energy does not affect the ion distribution.

Lens

When we did TOF experiments in the preparation chamber, the ion count changed by two orders of magnitude when varying the lens to grid voltage ratio from 0 to 1, and we found a clear maximum at $V_{lens}/V_{neg} = 0.5$ (Fig. 3.10a). Nevertheless, after connecting the two chambers through the constriction we could not see similar such a big impact on the count-rate by the lens. One possibility could be that the lens at the voltages we apply focuses the beam, but it never collimates the beam. Having said that, we still expected to observe some partial collimation along the axis of the lens, because the ions entering the lens are on diverging trajectories. Therefore, we were confused as to why we do not observe any clear change with varying the lens voltage. To have a better understanding of the beam optics, I decided to run a Comsol simulation.

The Comsol simulation of the D^- ions trajectories when $V_{lens} = -650$ V is shown in Fig. 3.16a. A total number of 2000 particles with no initial velocities were released from the grid. The grid voltage was set to -1000V and lens voltage was swept over -1000 V to +2000 V. In the simulation, at positive voltages the focusing effect was not as strong, and no partial collimation was observed unless going to voltages of around 2500V. However, at these posi-

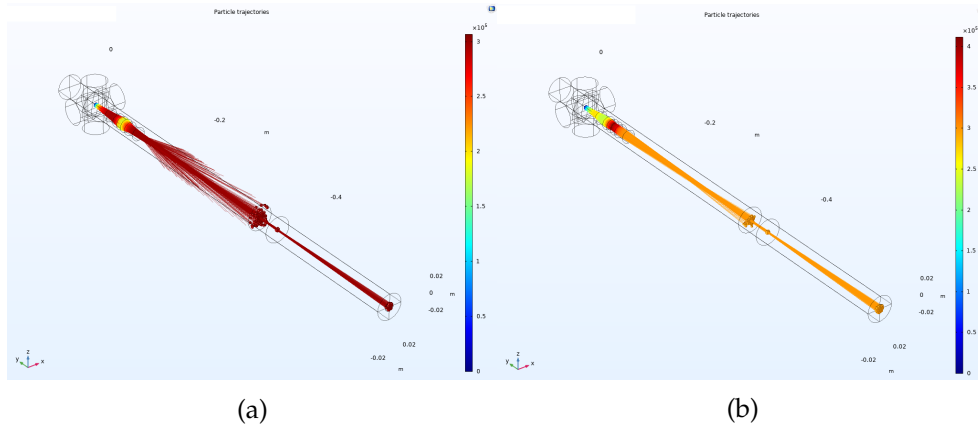(a)   (b)

Figure 3.16: **(a)** Simulation of the D$^-$ ions trajectories for $V_{neg} = 1000$ V and $V_{lens} = -650$ V. **(b)** Simulation of the D$^-$ ions trajectories for $V_{neg} = 1000$ V, $V_{lens} = 1000$ V and the first lens cylinder $V_1 = -400$ V (grounded in **(a)**).

tive voltages, in practice, the MCP gets flooded by the background electrons which is not desirable. Therefore, I mainly focused on the negative regime. At the end of the tube was placed a particle detector which counts the total number of particles hitting its surface. The detector was placed at 50 cm from the grid, with a diameter of 1 cm to mimic the MCP[13]. In Fig. 3.17a the count per experiment (meaning one grid pulse) of the D$^-$ ions alongside the simulation result is depicted. The simulation suggests that a lens voltage of around -670 V ($V_{lens}/V_{neg} = 0.67$) should produce the best partial collimation and the count-rate should be orders of magnitude more than when the ratio is 0.3 for example. However, in experiment, the lens at best boosts the D$^-$ ion count-rate by a factor of 2 at $V_{lens}/V_{neg} = 0.55$.

We also have the possibility to apply a nonzero voltage to the first cylinder of the lens (Fig. 3.18). To see if a better collimation could be produced using the first, as well as the middle cylinder, I also simulated a voltage sweep on these two cylinders. In Fig. 3.16b the simulated D$^-$ trajectories are depicted for $V_1 = -400$ V (first cylinder) and $V_{lens} = 1000$ V. In Fig. 3.17b the result of the simulation for different combinations of V_1 and V_{lens} is shown. This figure shows that a combination of -400 V and +1050 V to the first and the middle cylinder respectively should produce the best partial collimation even better focusing than the single cylinder lens by a factor of 2. Nevertheless, like the one cylinder configuration, the experimental result did not follow the simulation. The D$^-$ ion count-rate did not increase and the TOF became very noisy.

---

[13] Although a more accurate distance from the grid would have been 48 cm. However, it does not make a massive difference since particles passing through the constriction are almost collimated in the length scale of the constriction which is 3 cm.
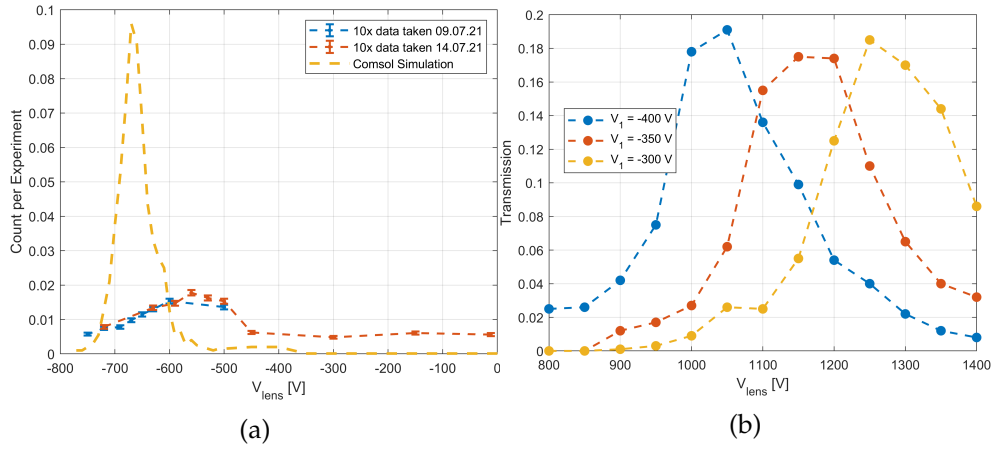
Figure 3.17: **(a)** Lens effect. Comparison between the experimental data and the simulation. **(b)** Simulating the use of the first two lens cylinder. V_1 denotes the first cylinder, and V_{lens} denotes the middle cylinder as before. Like the one lens configuration, the experimental data did not produce similar results to the simulation.
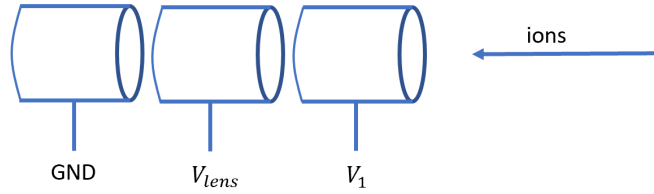

Figure 3.18: Schematic illustration of the lens in relation to the double lens configuration.

Grid Negative Pulse

As I mentioned in Sec. 3.3 increasing the grid negative pulse was the reason we started to detect particles. Therefore, we already expected the counts to increase with V_{neg}. Fig. 3.19a shows the results of three different measurements. The reason why we did this measurement several times was to make sure of the results as H$^-$ count was diminishing over time due to the hydrogen supply depletion. This depletion can be seen in H$^-$ count-rate in Fig. 3.19a comparing the data from 02.08 and 23.07 while for D$^-$ no depletion is observed. The effect of grid negative pulse on the peaks widths was also investigated. Fig. 3.19b illustrates that in general the peaks widths increase with V_{neg} specially for H$^-$. Hence it seems that the small dip of two of the data set for D$^-$ peaks widths around $V_{neg} = 300$ V is due to lack of sufficient statistics.
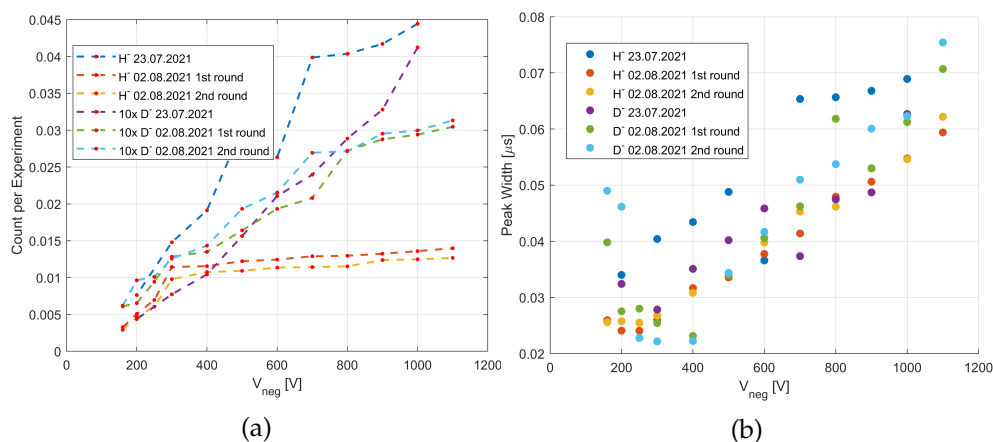
Figure 3.19: **(a)** Dependence of the H^-, and D^- count-rate on the grid negative pulse. Three experiments are presented here. Comparing the order of the experiments we can notice the depletion in the hydrogen supply. **(b)** The peaks widths in **(a)** as a function of the grid negative pulse. We can notice the monotonic increase in the width.

New E-Gun

As discussed in Chap. 2, the idea was to add another e-gun so that we set one e-gun around 40 eV, and the other one around 4 eV, and investigate the DEA process. I did this test after adding the second e-gun, but no negative ion counts were detected, neither H^- nor D^-.

When we set the two e-guns to around 200 eV, however, we observe that the negative ion count from the two e-guns add up. Therefore, the best operation of the source is when both e-guns are set to around 200 eV, as 200 eV was proved the optimum electron energy for D^- production with a single e-gun. It is also interesting to note that the two e-guns do not have identical contribution to the negative ion production. In fact, the e-gun that shoots electrons laterally at the grid (90° e-gun) provides $38 \pm 1\%$ while the straight e-gun provides $62 \pm 1\%$ of the counts.

Fig. 3.20a shows the effect of the rise in the emission current on the count-rate. The H^- peak increased by a factor of 10 when the emission currents of the two e-guns were raised from 30 μA to 1000 μA. This figure also shows that all the other peaks had disappeared. This happened gradually after we vented the chamber with 1.9 bar of hydrogen. Even though we replaced back the deuterium bottle, and also vented the chamber with 2 bar of deuterium for two days, we could never retrieve the D^- ion peak. Venting the chamber with 1.9 bar of hydrogen resulted in the diffusion of hydrogen into the grid. This could have altered the surface properties of the grid, and perhaps that is why we could never retrieve the D^- peak. In addition to the D^- peak, all

(a)   (b)
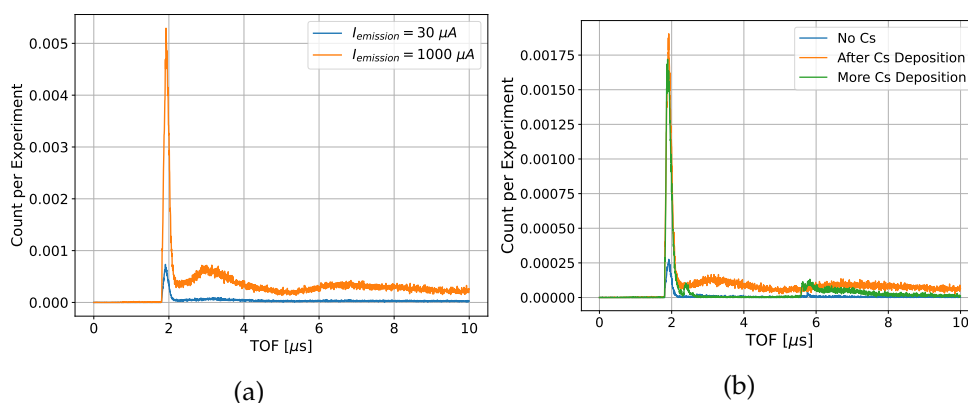
Figure 3.20: **(a)** TOF signal after installing the two new e-guns. Increasing the the emission currents from 30 μA to 1000 μA resulted in a tenfold increase in the H$^-$ peak. **(b)** Comparing the TOF signal before and after Cs deposition. The orange curve shows the TOF instantly after Cs deposition while the blue curve is just before it. Comparing the two, we see an increase in by more than a factor of 6. The green curve shows the TOF after more Cs deposition. The D$^-$ peak can be noticed making recovery.

the other peaks also had diminished. This diminishing can be explained by the hydrogen and water vapor supply depletion. However, after adding the new e-gun which results in water vapor adsorption, only the hydrogen peak recovered as can be seen in Fig. 3.20a.

After Cs deposition, I also investigated the focusing behavior of the e-guns and changed the $V_{Wehnelt}/V_{bias}$ ratio from 1.041 up to the maximum possible. 1.041 is the ratio determined by the Comsol simulation of the e-gun that produces the best focusing at the grid. For example, to have an emission current of 30 μA from the 90° e-gun, $V_{Wehnelt}/V_{bias} = 1.31$ is the maximum ratio we can have. The higher the emission current, the lower is the maximum ratio. Fig. 3.21a shows the H$^-$ and D$^-$ ions count versus the emission current of the two e-guns. This result suggests that larger $V_{Wehnelt}/V_{bias}$ ratios create more focused electron beams. Fig. 3.21b also shows the TOF signal for this measurement. Comparing these TOF signals with Fig. 3.20a, we see that more peaks have appeared in the TOF. Since this measurement was carried out after Cs deposition, this means that the Cs film has changed the adhesive ability of the surface in relation to deuterium and water vapor.

Cs Dispenser

The dispenser activates around 4.7 A. First, I increased the current with the rate of 0.4 A/min to 6 A and stayed there for 15 minutes. Then, I turned off the current with the rate of 0.6 A/min. Fig. 3.20b shows how the TOF

signal looks like before and after this Cs deposition (the blue and the orange curves). Before the deposition, the H$^-$ ion count-rate was 0.0086 while after the deposition I obtained more than a sixfold increase to 0.0538. Roughly 20 hours after this test, the count-rate dropped by a factor of 2 due hydrogen supply depletion.

To see if the count-rate could be further increased, next, I activated the dispenser with 7 A for 20 minutes. Then, I reduced the current to 5 A and left the dispenser on for 10 hours; then, I reduced the current to zero. The green curve in Fig. 3.20b shows the TOF done two days after this deposition. Due to the great number of experiments that I did in those two days, we can not read much into the change in the H$^-$ peak. However, as mentioned in Sec. 3.3.2, it can be seen that the deuterium peak and the multiple peaks around 6 μs have started to appear again. In these measurements both e-guns emission currents were set to 30 μA. After Cs deposition, the highest D$^-$ ion count-rate was 0.0071 at the conditions below:

V_{neg} = 900 V, both e-guns V_{bias} = -192 V, $I_{emission}$ = 500 μA,

$V_{Wehnelt}$ maximum possible.

Before venting the chamber with hydrogen, the maximum count-rate was 0.0068 with these conditions:

V_{neg} = 900 V, V_{bias} = -192 V, $I_{emission}$ = 30 μA, $V_{Wehnelt}/V_{bias}$ = 1.05

Bear in mind that this count-rate was with only one e-gun and no Cs deposition. Hence, now with these additions, we should expect the D$^-$ ion count-rate to be higher. To further retrieve the D$^-$ ion peak, we can do more Cs evaporation, or simply replace the grid with a new one. It could also be that the deuterium adsorption kinetics is so slow that we need to wait longer for the deuterium supply to recharge. There is one evidence in favor of this theory when we compare Fig. 3.15a (taken with V_{neg} = 900 V) with Fig. 3.19a (taken with V_{bias} = -192 V). The data in Fig. 3.15a was taken on July 22 which is before all the data represented in Fig. 3.19a. Looking at the count-rate at V_{bias} = -192 V in Fig. 3.15a, we see that the count-rate is 0.0068 while at V_{neg} = 900 V in Fig. 3.19a the count-rate is around 0.003 for all the data. Hence we have a drop in the D$^-$ ion count-rate by a factor of 2. However, contrary to H$^-$, dropping of the D$^-$ ion count-rate was not constant. Hence the deuterium supply can partially and temporarily be depleted by our use, and the D$^-$ count-rate could be limited by the adsorption kinetics. If this theory is true, then we should expect the D$^-$ peak to further increase as time passes.
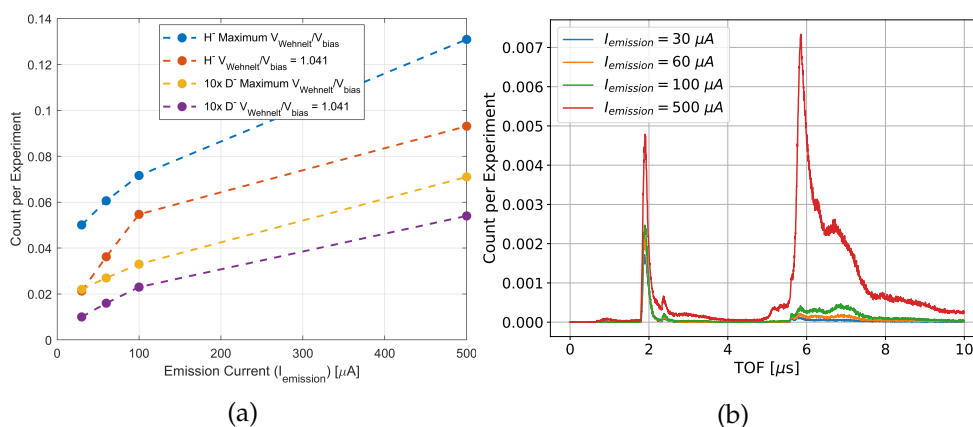
(a) (b)

Figure 3.21: **(a)** Dependence of the H$^-$, and D$^-$ count-rate on the two e-guns emission currents after Cs deposition. **(b)** TOF signals of the experiments shown in **(a)**.

3.4 Discussion

All experimental results point towards the surface production of D$^-$ ions. Here I will go through all the evidence one by one.

- The amount of ions produced through DEA must linearly depend on deuterium pressure. However, in our source, ion production does not depend on pressure at all. In contrast, if we go to pressures of the order of $\sim 10^{-5}$ mbar or higher, the TOF signal becomes noisier instead of becoming stronger.

- The presence of a strong H$^-$ peak alongside OH$^-$ and OD$^-$ peaks also strengthens the position of the surface production theory because there are no H$_2$, OH, or OD gas present in the chamber.

- The D$^-$ ion TOF linewidth[14] is of the order of 10 ns. The TOF simulation tells us that to have a TOF standard deviation of ~ 10 ns the ions must be within a couple hundred microns of the grid prior to the acceleration (Fig. 3.22a). If ions were created through DEA, the ions would have been created all over the chamber, and the TOF peaks would have had a long tail as shown in Fig. 3.22b.

- The cross-section of the DEA process has peaks at 4 eV, 10 eV, and 14 eV. Nevertheless, we observe that the ion production increases by two orders of magnitude when increasing the electron energy from 20 eV to 200 eV. We can explain this through the surface negative ionization

---

[14]The linewidth is defined as the fitting parameter of the Doniach-Sunjic fit which is roughly equal to the FWHM. It is also very close to the standard deviation of the Gaussian fit.
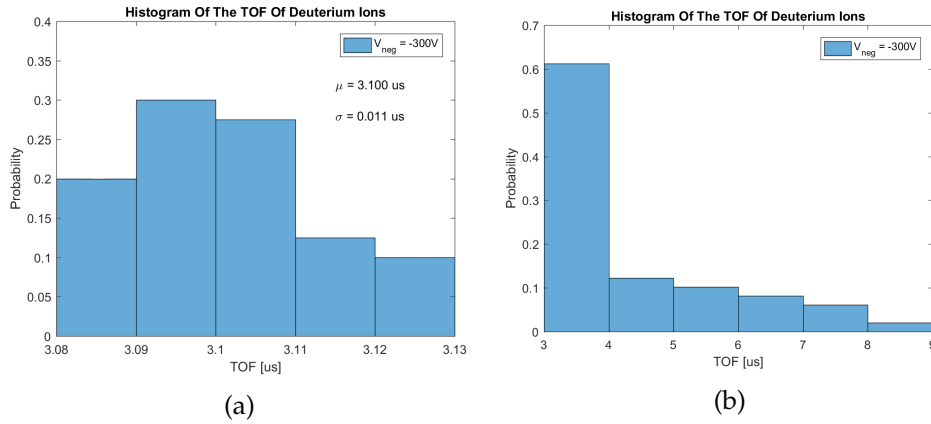
Figure 3.22: **(a)** TOF simulation with the grid negative pulse set to 300 V, when D$^-$ ions being initially distributed in the 300 μm radius of the grid. The standard deviation of the simulated TOF is derived to be 11 ns. **(b)** The same simulation as **(a)** with the difference that the ions were distributed in the 2 cm radius of the grid.

process. The adsorbed D, H, OH, and OD gain an extra electron on the grid surface, but they need some momentum to fly off the grid (Eq. 2.7). This momentum could be provided to the ions through electrons impact. Higher-energy electrons can transfer more momenta to the ions. Hence increasing the electron energy should produce more negative ions through such a surface process. As to why the ion production peaks around 200 eV, it could be that higher-energy electrons can knock out the extra electron of the ions upon their impact, hence reducing the ion production. This process sounds similar to the sputtering negative ion sources discussed in Sec. 2.2.1 apart from the fact that instead of positive ions, here electrons transfer the momentum to the surface-created negative ions.

• Cs deposition also increases the ion production. We know that Cs deposition on refractory metals like tungsten reduces the work function. Hence the impact of Cs deposition on our system can be explained by surface negative ionization theory of deuterium.

Chapter 4

Setup Development - the Control System and the Vacuum Components

4.1 Control System

In this chapter I am going to discuss the control system which has the task of read-out and controlling the electronics. This control system is also being used in trapped-ion experiments in TIQI. A detailed description on the control system can be found in [37]. The heart of the control system is an FPGA[1] development board called the Zedboard. It receives the MCP pulses and registers their times of arrival (timestamps) enabling us to form the TOF histogram with the precision of 4 ns which is the FPGA clock cycle.

It also produces 32 CMOS logic control signals. These 32 signals are then fed to a TTL breakout board where they are converted to TTL level voltages. These TTL signals are then used for controlling the electronics in the setup, e. g., the high voltage switch [30].

I divide the description of the control system into two sections: detection, and control.

4.1.1 Detection

Discriminator Board

The purple signal in Fig. 4.1 is an MCP pulse. These pulses vary in amplitude and width. To count these pulses we need to convert them into standard pulses so that every detection pulse looks alike with identical voltage levels. This task is done by the discriminator board. This board receives, and inverts the MCP pulse, amplifies it by a factor of 10 (the blue signal in

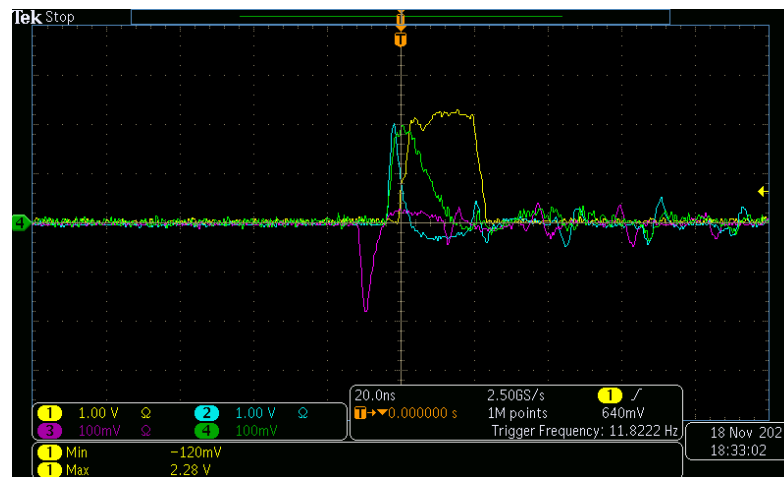---

[1]Field-programmable gate array.

Figure 4.1: Illustration of the MCP pulse (purple), after amplification (blue), after the RC filter (green), and in the output of the discriminator board (yellow).

Fig. 4.1), then passes it through an RC filter. The RC filter roughly attenuates the amplified pulse amplitude by a factor of 10 and also expands the pulse in time (the green signal). This pulse then goes into a comparator IC which compares the pulse with a reference voltage. The time expansion by the RC filter is necessary for the comparator IC to have the time to inspect the pulse. We can adjust the reference voltage with a potentiometer screw on the board. If the pulse goes above the reference voltage for 1 ns, a TTL pulse is produced in the output of the board (the yellow signal). There is also a latch mechanism in the comparator which latches the output pulse by 5 ns[2] so that the pulse is long enough (above 4 ns) to be counted by the Zedboard. The rise time and the fall time of the produced TTL pulses by the comparator are 2 ns.

The MCP pulses depend on its bias in terms of amplitude distribution and width. I chose to bias the MCP with 2.7 kV because it produces broad enough amplitude distribution for finding counting efficiency (See Sec. 4.1.1). The MCP pulses should be below 500 mV in the input of the discriminator board. This limit is imposed by the BJT amplification stage of the discriminator board. Hence I had to add a 10 dB attenuator before the discriminator board to bring the pulse level below 500 mV. After the 10 dB attenuator, the MCP pulses are 2 ns to 5 ns in width depending on the height of the pulse. The histogram of the MCP pulses height after the RC filter is shown in Fig. 4.2a. It shows that the pulses are distributed from 20 mV to 350 mV. Fig. 4.1 also shows that after the main MCP pulse there are also some oscillations.

---

[2]It means that the output is kept high for 5 ns after the input goes below the reference voltage.

These oscillations are 22 ns apart and the first oscillation is about 25% of the main peak in amplitude and they gradually die out in 200 ns. These oscillations are shorter in width and also for the vast majority of the MCP pulses they lie below the reference voltage (that I have set to 50 mV), so there is no concern as to counting a single pulse several times. To make sure that we do not have multiple counting at $V_{ref} = 50$ mV, I received all the MCP pulses (after the RC filter) higher than 50 mV, and analysed the discriminator output. Fig. 4.2b shows that out of 400 MCP pulses above 50 mV, 360 of them resulted in a single TTL pulse and 40 of them failed to generate anything. This shows that we do not have multiple counting at $V_{ref} = 50$ mV[3]. Fig. 4.3a also shows the histogram of the counted discriminator pulses lengths. More than 95% of these pulses are 20 ns to 25 ns long.

The oscillations are neither caused by the discriminator board, nor the MCP bias circuit [31]. They can not be brought about by impedance mismatch either as the oscillations timing is not dependent on the cables lengths. One theory could be that these oscillations are due to some internal reflection effect within the MCP. The MCP we are using is actually a stack of three MCPs called a Z-Stack MCP. It could be that the avalanche of the electrons partially back-scatter at the surfaces of the stacked MCPs, and as a result create secondary pulses with fixed intervals.

Counting Efficiency

A relevant measurement to do with the discriminator board was to see how counting efficiency is related to the reference voltage of the discriminator board. Counting efficiency is the ratio of the number of counted pulses by the control system to the total number of pulses generated by the MCP. What I did was to change the reference voltage and read the measured number of counts in a fixed detection window of 5 μs. I did this measurement with two different grid negative pulses $V_{neg} = 260$ V and 110 V and two different V_{lens}/V_{neg} ratios. The result is displayed in Fig. 4.3b. The measurement on the count-rate fits with an exponential decay of $c = 0.1875 \exp\{(-V_{ref} \, [\text{mV}]/92.87 \text{ mV})\}$. This measurement shows that the counting efficiency is approximately $\exp\{(-50/92.87)\} = 58\%$ at $V_{ref} = 50$ mV. If the reference voltage is set below 50 mV, the exponential fit slowly diverges from the experimental count-rate. As the reference voltage is set

---

[3]The TTL pulses of the discriminator go to a buffer board called the PMT breakout board, where TTL pulses are buffered, then go to the ADC of the Zedboard. For the PMT breakout board to create TTL pulses the discriminator TTL pulses need to reach 2 V. For the Zedboard to count these TTL pulses, they need to be at least 4 ns in width. I used these two criteria to count the TTL pulses of the discriminator board. For example, the bin of zero count in the histogram of Fig. 4.2b represents pulses that do not reach 2 V, or reach 2 V but are shorter than 4 ns.
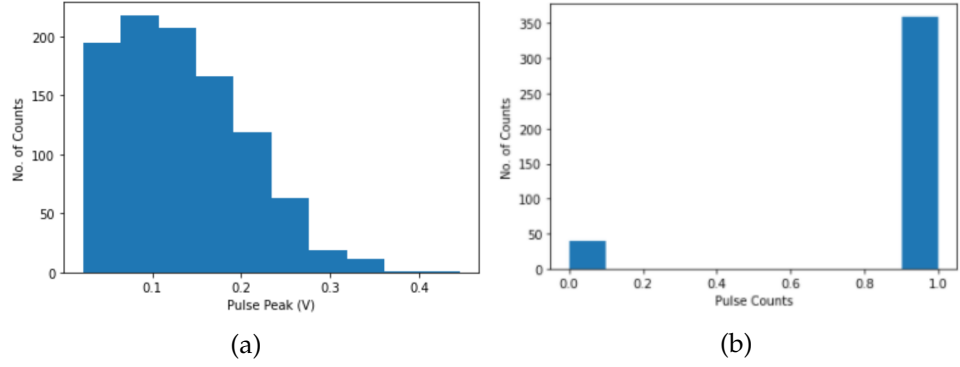
(a)

(b)

Figure 4.2: **(a)** Distribution of the MCP pulses after the RC filter. **(b)** Histogram of the number of counted pulses per detected pulse at $V_{MCP} = 2.7$ kV, and $V_{ref} = 50$ mV. No multiple counting was observed.
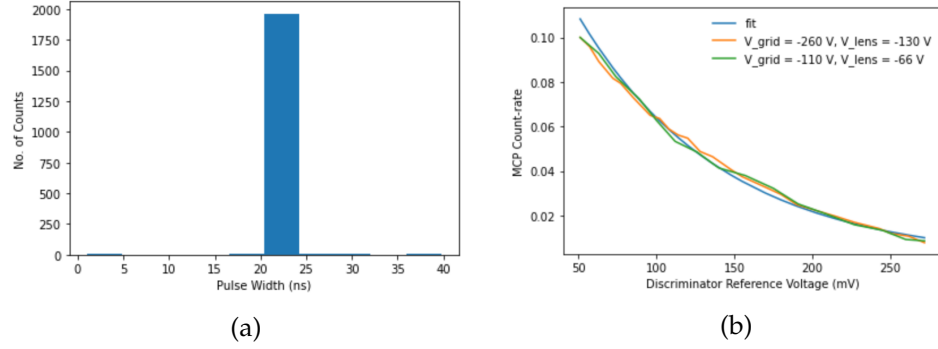

(a)

(b)

Figure 4.3: **(a)** Histogram of the counted discriminator pulses lengths. More than 95% of these pulses are 20 ns to 25 ns long. **(b)** Count-rate as a function of the discriminator reference voltage. This measurement was done over two different conditions to make sure that the result was not dependent on the other conditions than the reference voltage. The count-rate for both conditions fit $c = 0.1875 \exp\{(-V_{ref} \, [\text{mV}]/92.87 \, \text{mV})\}$.

to values below 50 mV, the MCP pulse oscillations become comparable with the reference voltage and result in multiple counting by the control system.

To know the total detection efficiency, the detection efficiency of the MCP for H^-, D^-, and electrons needs to be known too. Based on the information provided by the MCP manufacturer, Tectra, the MCP detection efficiency for electrons is between 50% to 85%, and for positive ions between 5% to 85%. For negative ions no detection efficiency has been provided by the manufacturer. However, if the average MCP detection efficiency for all the particles is taken to be 85%, it means that $0.85 \times 58\% = 49.3\%$ of the arrived particles at the MCP is counted.
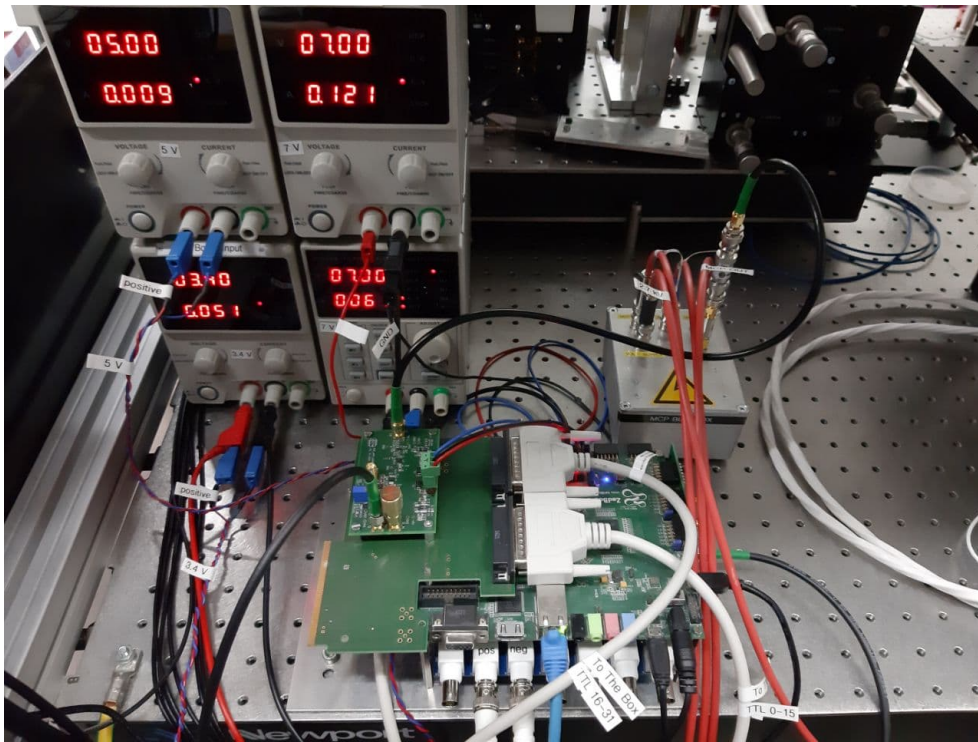
Figure 4.4: Picture of the control system.

4.1.2 Control

FMC and TTL Breakout Boards

The FMC board connects to the Zedboard enabling us to use the Zedboard-created control signals. It outputs the signals through two db25 connectors, each containing 16 control signals and 9 ground pins. One of the db25 outputs is connected to the DAC-Switch box (Sec. 4.1.2), and the other one is connected to the TTL breakout board (also called the optoisolator board) where the control signals are first isolated from the Zedboard using optoisolator ICs (to suppress the high frequency digital noise of the Zedboard), and then connected to BNC connectors through buffer ICs. We currently use two of these BNCs to control the high voltage switch that switches the grid voltage.

DAC-Switch Box

We could think of two reasons as to why we need a box with which we can sweep and switch voltages. One is to trap deuterium ions, and the other is to control the beam optics, e. g., the deflection plates. To trap the deuterium ions, one way could be to decelerate the deuterium ions and instantly switch
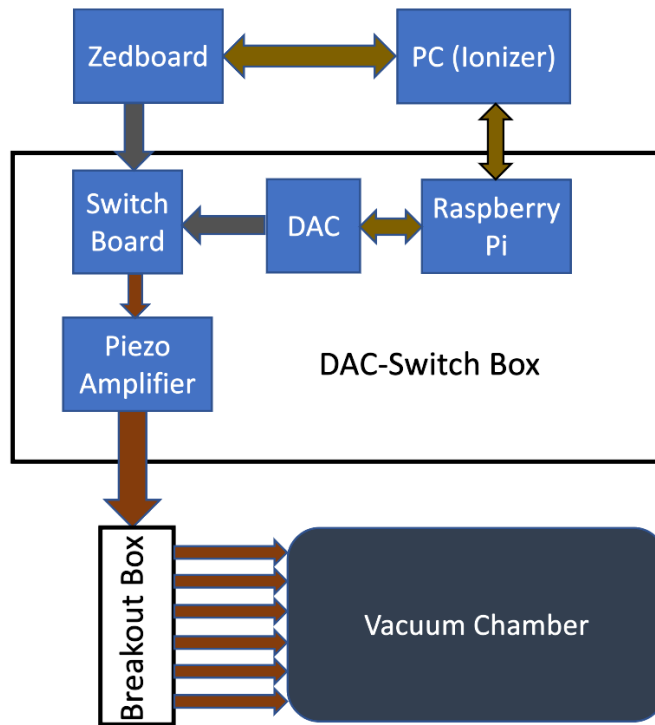
Figure 4.5: Schematic illustration of the DAC-Switch box. Two-sided arrows represent communication. Gray arrows represent the inputs to the switch board where the switching by the multiplexers happens.

the trap axial potential to trap the ions. This required us to use high speed multiplexers that could be controlled by the logic signals coming from the Zedboard through the db25 connection. This enables us to control the timing of switching through the Zedboard. In Fig. 4.5 the schematics of the DAC-Switch box is displayed. The logic signals from the Zedboard go to an array of optoisolators for noise cancellation, then fed to the multiplexers. To create the input voltages to the multiplexers, a Raspberry Pi microcontroller is used to control a DAC which can output [-10, 10] V. The Raspberry Pi control over the DAC enables us to sweep the DAC voltages. This Raspberry Pi DAC voltage control is linked with the Zedboard (which controls the TOF experiment) through "Ionizer" software[4]. The 2-D voltage sweep in Fig. 3.12a, for example, was performed with this method.

These voltages coming from the DAC are then connected to the multiplexers. The TTL signals coming from the Zedboard enable us to switch among them

---

[4]Ionizer is developed at TIQI. This software provides the GUI to control the experiments by the FPGA system. Through the plug-in feature in Ionizer we can link the experiment with other controllers like the Raspberry Pi in our case.

at will[5]. The outputs of these multiplexers are fed to a piezo-amplifier which is a voltage amplifier with a factor of 25. Then, the output is available as a db9 connector on the box. The piezo-amplifier is powered up through a socket on the box by the AC line. The other components of the box are powered up by a power supply unit which outputs -5 V, +5 V, 12 V. Since the piezo-amplifier has 6 outputs, and the multiplexers are 4-channel, we are only using 24 DAC channels out of 40. The remaining 16 DAC channels are connected to two 8-channel multiplexers, but their outputs are not used. However, these two multiplexers outputs can also be outputed from the box in a later upgrade.

The box can be biased by any desired voltage through an SHV feedthrough on the box. This gives us the ability to have [-250, 250] V voltage swing around the desired bias. The box outputs are given to a breakout box. The breakout box receives the DAC-Switch box outputs through a db9 connection and breaks them out to 6 separate banana/SHV connectors.

4.2 Vacuum Components

Here I will provide some further information on the e-gun and Cs dispenser installation in the chamber.

4.2.1 E-Gun

In the previous chapters I have already touched on the addition of the new e-gun. What we actually did was to design a new e-gun, remove the previous e-gun [31], and instead add two newly designed e-guns together with pairs of deflection plates to be able to stir the electron beam. Fig. 4.6 shows the new design.

As pointed out in Sec. 3.3.2 the $V_{Wehnelt}/V_{bias}$ ratio is limited from above depending on the emission current. This is a mistake in the new e-gun design. The e-gun Wehnelt cylinder opening in our design is 2 mm. There is, however, a similar e-gun being used in the "Molecules Project" at TIQI that has an opening of 3 mm, and they do not have any problem with increasing the $V_{Wehnelt}/V_{bias}$ ratio. Hence if we wish to increase the $V_{Wehnelt}/V_{bias}$ ratio further for better focusing, we have to rectify the e-gun design and replace the current e-guns with new ones.

---

[5]Ionizer enables us to do the switching manually. TTL signals number 16 to 31 are allocated for this. Switching can also be implemented within the TOF experiment, for example, 5 μs after the grid switching. We can also define a time variable for the multiplexer switching that could be changed by Ionizer. To do this, the experiment C code needs some alterations.
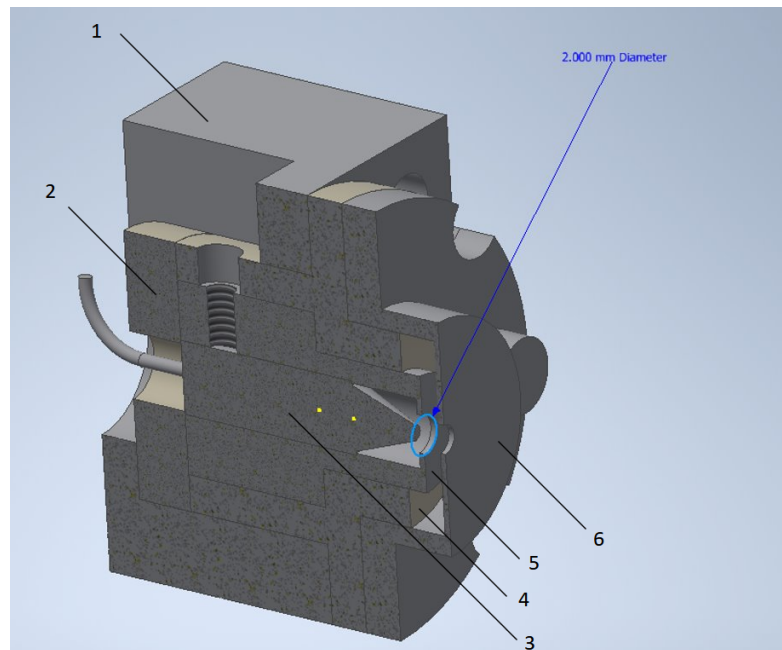
Figure 4.6: CAD of the new e-gun in half view. 1) E-gun mount; 2) ceramic (macor) disc spacer; 3) e-gun cathode containing the Ta disc; 4) ceramic cylindrical spacer; 5) Wehnelt cylinder; 6) ground disc. The opening of Wehnelt cylinder (ground disc) is 2 (1.5) mm.

4.2.2 Cs Dispenser

The wire-shaped SAES getters Cs dispenser that we used is 12 mm long with 10 mm flat terminals on the sides (Fig. 4.7a). It contains 5.2 mg of caesium in the form of caesium chromate (Cs_2CrO_4) salt. As currents above 4.7 A run through the dispenser, caesium chromate heats up to 550°C to 850°C, and a reduction reaction starts between the chromate and the St 101 alloy[6], and subsequently causes the caesium to evaporate from the slit in the middle of the dispenser.

To install the dispenser inside the chamber, we designed a mount. Fig. 4.7b shows the CAD of the mount. It is designed to be installed on the alumina rods that hold the other components as well; meaning the e-gun, and the deflection plates (Fig. 4.8). Fig. 4.9a, illustrates how different components are installed on the alumina rods. The alumina rods are supported by the groove grabbers. The groove grabbers are fixed in place by clinging onto the grooves of the close coupler. Fig. 4.9b shows the installed dispenser. The dispenser has an angle of roughly 20° to the tube axis. This angle

---

[6]St 101 alloy is a non-evaporable getter (NEG) made of zirconium, cobalt, and one or more components selected among yttrium, lanthanum, or rare earths.
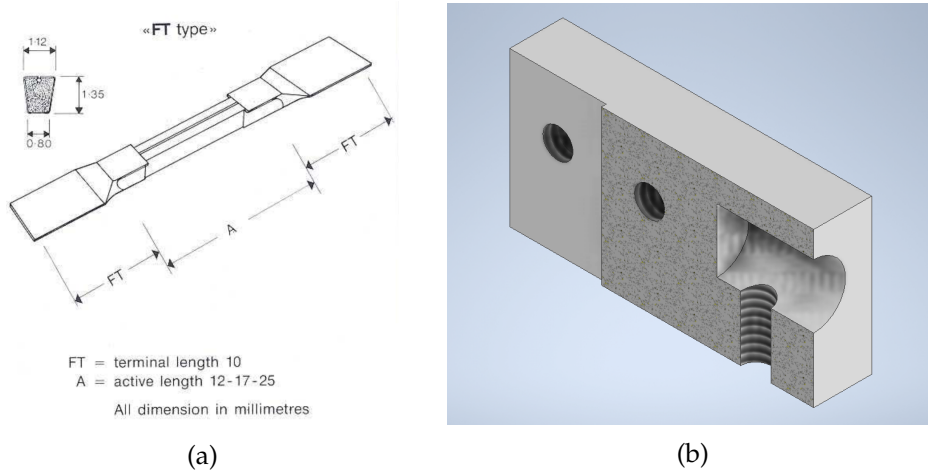
Figure 4.7: **(a)** Drawings of the Cs dispenser. We are using one with $A = 12$ mm. **(b)** CAD of the dispenser mount in half view.
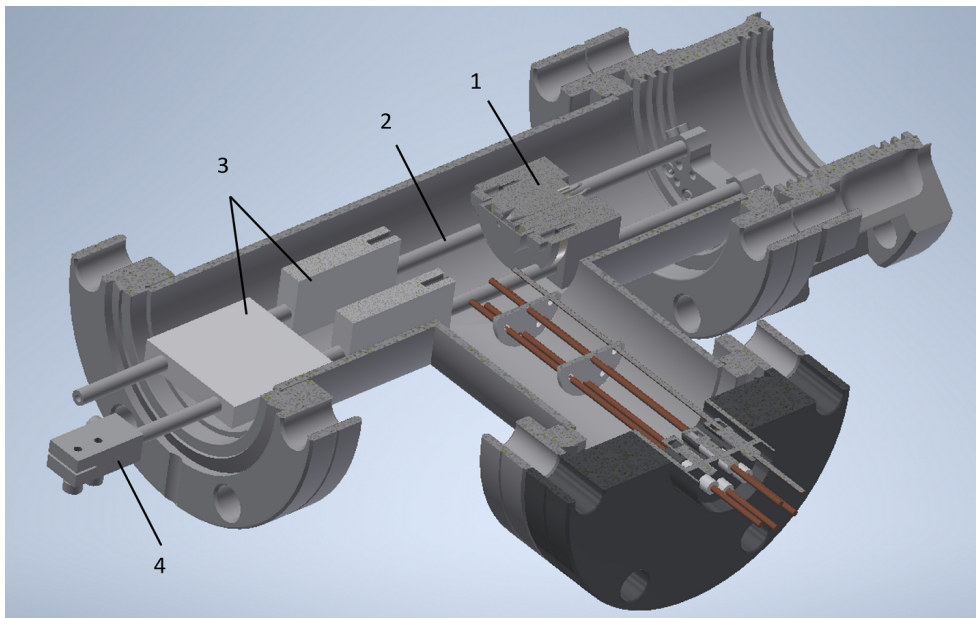

Figure 4.8: CAD of 1) the e-gun, 2) alumina rod, 3) deflection plates, and 4) dispenser mount assembly in half view.

(a)   (b)
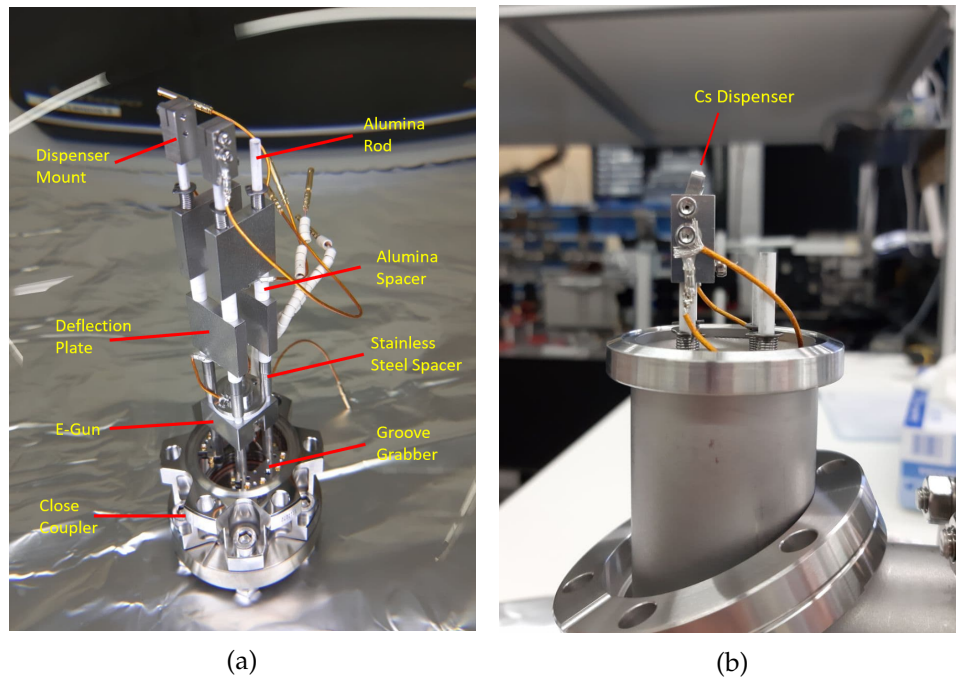
Figure 4.9: **(a)** Assembly of the e-gun arm. **(b)** Mounted Cs dispenser.

(a)   (b)
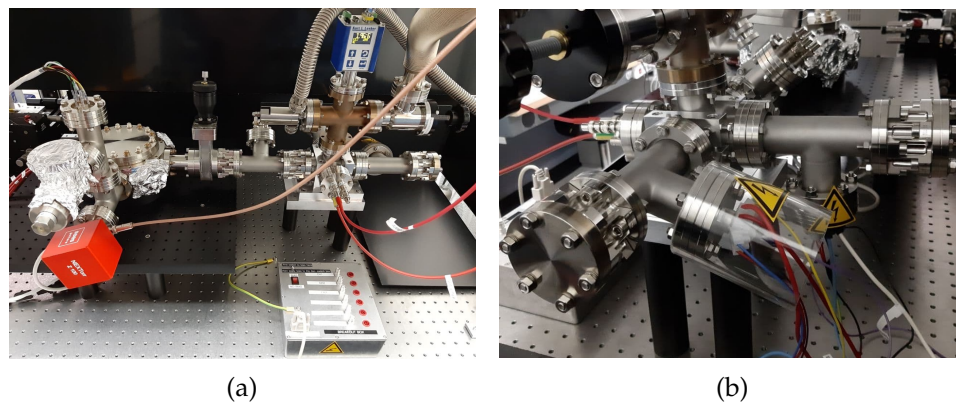
Figure 4.10: **(a)** The final vacuum chamber setup. **(b)** The two e-gun arms installed in place.

is necessary to focus the caesium vapor onto the center of the grid. The dispenser is installed in the vacuum chamber arm which is straight to the ion beam direction, i. e., it directly faces the grid. The other e-gun and deflection plates are installed in the 90° chamber arm. Fig. 4.10a illustrates how the whole vacuum setup looks like after the new additions, and Fig. 4.10b shows a zoomed-in image of the two e-gun arms.

Chapter 5

Outlook

5.1 Current Position

During the time that I worked on this project, we managed to connect the preparation chamber to the trap chamber, and pass some of the produced negative ions through the differential pumping constriction. We observed that increasing the grid negative voltage from 100 V to 1000 V raises the D^- ion count-rate by a factor of 10. Increasing the electron beam energy from 20 eV to 192 eV increases the count-rate 100 times. Increasing the e-gun emission current from 30 μA to 1000 μA raised the count-rate 10 times. Cs deposition increased the count-rate by more than 6 times. Finally, addition of the 90° e-gun increased the count-rate by a factor of 1.6.

Besides, we also have the depletion of the source for hydrogen. Hence we can not state a final amount for the H^- ion count-rate. For the deuterium, however, we do not have depletion, but we still observed partial drop in the D^- ion count-rate perhaps due to slow adsorption kinematics. Nevertheless, this drop recovers when we do not use the source for some weeks. The best count-rate that we obtained from D^- ions was in the e-gun V_{bias} sweep experiment where we had a count-rate of 0.0068 at $V_{neg} = 900$ V, and $V_{bias} = -192$ V, $I_{emission} = 30$ μA.

After we replaced the deuterium bottle with hydrogen, and vented the chamber with 1.9 bar of hydrogen, we never recovered the D^- ion count-rate. However, after caesium deposition on the grid, the D^- ion peak has started recovering. Finally, the highest count-rate gained with two e-guns and Cs deposition was 0.0071 for $V_{neg} = 900$ V, $V_{bias} = -192$ V, $I_{emission} = 500$ μA and maximum $V_{Wehnelt}$ possible.

5.2 Outlook

To see if the discussed D^- ion production setup works, the next step is to try to trap the D^- ions. To do so, we need to devise a deceleration scheme for the ions as they reach the trap chamber to bring the ion energy down to ~ 1 eV. At ~ 1 eV energy level we would have enough time to switch the trap electrodes[1].

One of the challenges that we will face in the trapping of the D^- ions is that the production rate (i. e., D^- ions produced per acceleration pulse) is not large[2]. To further increase the production rate, we have a few options. Here I put forward two suggestions that need the least amount of modifications to the current setup.

One option is to convert the source into a Cs sputtering source as depicted in Fig. 2.5. What we need to do is to replace the grid with a TiD_2 cathode, design and add a tungsten ionizer for the Cs ionization. The additional advantage of this source is that with choosing the right cathode, it can be used as a general negative ion source to make almost any desired negative ions [23].

The other option is to use the pulsed laser approach (Sec. 2.3). Again, we need to replace the grid with a TiD_2 cathode; then, irradiate the cathode with a pulsed laser of the right pulse energy. The TiD_2 target is metallic with a low work function (specially if Cs vapor added), and also in the formed plasma of Ti and D, deuterium would have a much stronger inclination to electron attachment in comparison with titanium[3]; therefore, above some certain pulse energy we may expect that D^- ions be produced.

Although the pulsed laser approach needs the least amount of modifications to the vacuum chamber, this approach to make negative ions is not a well-known technique, and apart from knowing that the target material and laser pulse energy matter, it is not yet clear that how this method works. For example, for a laser pulse energy density of 1 J/cm^2 the plasma temperature will be of the order of $k_B T = 10$ eV [38]. These temperatures could be so high that in the thermal collisions between the created D^- ions and other particles, the ions lose their electrons. This was not an issue for osmium atom, but it could be for deuterium, especially that the electron affinity of deuterium (= 0.7546 eV) is smaller than osmium (= 1.0778 eV).

---

[1]For more information on the trapping please refer to the forthcoming master's thesis of Georg Engin-Deniz.

[2]A large production rate is considered to be orders of magnitude above 1.

[3]Electron affinity of deuterium is 0.7546 eV while for titanium it is only 0.0755 eV.

Bibliography

[1] G. F. M. Tomassi. Concept analysis and fabrication of an ion trap to couple negative and positive ions. Master's thesis, Trapped Ion Quantum Information Group, ETHZ, 2021.

[2] P. O. Schmidt, T. Rosenband, C. Langer, W. M. Itano, J. C. Bergquist, and D. J. Wineland. Spectroscopy using quantum logic. *Science*, 309, 2005.

[3] G. Schneider, A. Mooser, M. Bohman, N. Schön, J. Harrington, T. Higuchi, H. Nagahama, S. Sellner, C. Smorra, K. Blaum, Y. Matsuda, W. Quint, J. Walz, and S. Ulmer. Double-trap measurement of the proton magnetic moment at 0.3 parts per billion precision. *Science*, 358, 2017.

[4] C. Smorra, S. Sellner, M. J. borchert, J. A. Harrington, t. Higuchi, H. Nagahama, t. tanaka, A. Mooser, G. Schneider, M. bohman, K. blaum, Y. Matsuda, c. ospelkaus, W. Quint, J. Walz, Y. Yamazaki, and S. Ulmer. A parts-per-billion measurement of the antiproton magnetic moment. *Nature*, 550, 2017.

[5] E. G. Myers. CPT tests with the antihydrogen molecular ion. *Phys. Rev. A*, 98, 2018.

[6] M. Bacal and M. Wada. Negative ion source operation with deuterium. *Plasma Sources Sci. Technol.*, 29(3), 2020.

[7] Bailey L. Donnally, Thomas Clapp, William Sawyer, and Margaret Schultz. Metastable hydrogen atoms produced in charge exchange. *Phys. Rev. Lett.*, 12, 1964.

[8] I. Cadez, R. I. Hall, M. Landau, F. Pichou, and C. Schermann. Dissociative electron attachment to vibrationally excited H_2 and D_2 molecules: the 14 ev process. *J. Phys. B: At. Mol. Opt. Phys.*, 21(19), 1988.

[9] K. N. Leung, K. W. Ehlers, and R. V. Pyle. Effect of wall material on H^- production in a multicusp source. *Appl. Phys. Lett.*, 47(3), 1985.

[10] D. A. Skinner, A. M. Bruneteau, C. Courteille P. Berlemont, R. Leroy, and M. Bacal. Isotope effect and electron-temperature dependence in volume H^- and D^- ion sources. *Phys. Rev. E*, 48(3), 1993.

[11] E. Krishnakumar, S. Denifl, I. Čadež, S. Markelj, and N. J. Mason. Dissociative electron attachment cross sections for H_2 and D_2. *Phys. Rev. Lett.*, 106(24), 2011.

[12] M. Allan and S. F. Wong. Effect of vibrational and rotational exictation on dissociative attachment in hydrogen. *Phys. Rev. Lett.*, 41(26), 1978.

[13] J. R. Hiskes. Cross sections for the vibrational excitation of the $H_2 X^1\Sigma_g^+(v)$ levels generated by electron collisional excitation of the higher singlet states. *Journal of Applied Physics*, 70(7), 1991.

[14] S. K. Srivastava and O. J. Orient. Polar dissociation as a source of negative ions. *AIP Conference Proceedings*, 111, 1984.

[15] C. Jacquot, J. Pamela, D. Riz, and Yu. Belchenko. Negative ion production in large volume source with small deposition of cesium. *Review of Scientific Instruments*, 67(3), 1996.

[16] J. R. Hiskes, A. Karo, and M. Gardner. Mechanism for negative-ion production in the surface-plasma negative-hydrogen-ion source. *Journal of Applied Physics*, 47(9), 1976.

[17] B. Rasser, J. N. M. Van Wunnik, and J. Los. Theoretical models of the negative ionization of hydrogen on clean tungsten, cesiated tungsten and cesium surfaces at low energies. *Surface Science*, 118(3), 1982.

[18] Ming L. Yu. Work-function dependence of negative-ion production during sputtering. *Phys. Rev. Lett.*, 40(9), 1978.

[19] W. G. Graham. Negative hydrogen ion production by low energy hydrogen atom bombardment of surfaces. *Physics Letters A*, 73(3), 1979.

[20] P. J. Schneider, K. H. Berkner, W. G. Graham, R. V. Pyle, and J. W. Stearns. H^- and D^- production by backscattering from alkali-metal targets. *Phys. Rev. B*, 23(3), 1981.

[21] J. R. Hiskes and P. J. Schneider. Formation of H$^-$ and D$^-$ ions by hydrogen and deuterium particle backscattering from alkali-metal surfaces. *Phys. Rev. B*, 23(3), 1981.

[22] Eckstein W. Mechanism for negative-ion production in the surface-plasma negative-hydrogen-ion source. *IPP-Report IPP 17/12 Max-Planck-Institut, Plasmaphysik*, 2009.

[23] R. Middleton. A negative ion cook book. 1989.

[24] J. Blahins, T. Leopold, A. Apsitis, U. Berzins, A. Ubelis, J. Rohlén, D. Lu, and D. Hanstorp. Operating a cesium sputter source in a pulsed mode. *Review of Scientific Instruments*, 91(2), 2020.

[25] R. McAdams, R. F. King, G. Proudfoot, and A. J. T. Holmes. Pure and cesiated cw volume source performance at the culham ion source test stand. *AIP Conference Proceedings*, 287, 1992.

[26] K. W. Ehlers and K. N. Leung. Multicusp negative ion source. *Review of Scientific Instruments*, 51(6), 1980.

[27] Sergey Kondrashev, E Beebe, T Kanesue, M Okamura, and R Scott. Study of ion generation by a ps-laser for external injection into electron beam ion source. *https://doi.org/10.2172/1784483*, 2021.

[28] L. Torrisi, S. Gammino, L. Ando, and L. Laska. Tantalum ions produced by 1064 nm pulsed laser irradiation. *Journal of Applied Physics*, 91(7), 2002.

[29] D. Rodríguez, V. Sonnenschein, K. Blaum, M. Block, H.-J. Kluge, A. M. Lallena, S. Raeder, and K. Wendt. Production of negative osmium ions by laser desorption and ionization. *Review of Scientific Instruments*, 81, 2010.

[30] M. Simoni. Design, assembly and measurements for a uhv chamber to be used for D$^-$ ions trapping. Master's thesis, Trapped Ion Quantum Information Group, ETHZ, 2021.

[31] S. Koch. Production and control of deuterium anions and outlook to quantum logic spectroscopy-based tests of cpt violation. Master's thesis, Trapped Ion Quantum Information Group, ETHZ, 2021.

[32] A. Hodgson and S. Haq. Water adsorption and the wetting of metal surfaces. *Surface Science Reports*, 64(9), 2009.

[33] Elisa Albanese, Cristiana Di Valentin, and Gianfranco Pacchioni. H_2O adsorption on WO_3 and WO_{3-x} (001) surfaces. *ACS Appl. Mater. Interfaces*, 9, 2017.

[34] R. Dobrozemsky, S. Menhart, and K. Buchtela. Residence times of water molecules on stainless steel and aluminum surfaces in vacuum and atmosphere. *J. Vac. Sci. Technol. A*, 25, 2007.

[35] H. F. Dylla. The problem of water in vacuum systems. *CERN Accelerator School*, 2006.

[36] P. Chiggiato. Materials and properties iv outgassing. *CERN Accelerator School (CAS) on Vacuum for Particle Accelerators*, 2017.

[37] B. Keitch, V. Negnevitsky, and W. Zhang. Programmable and scalable radio frequency pulse sequence generator for multi-qubit quantum information experiments. *arXiv:1710.04282*, 2017.

[38] J. Haverkamp, R. M. Mayo, M. A. Bourham, J. Narayan, C. Jin, and G. Duscher. Plasma plume characteristics and properties of pulsed laser deposited diamond-like carbon films. *Journal of Applied Physics*, 93(6), 2003.